◇ Monograph Excerpt ◇

Matter Antimatter Fluctuations

search, discovery and analysis of Bs flavor oscillations

Nuno Leonardo

Complete work published as:
Analysis of B_s oscillations at CDF, MIT Thesis (2006)
Matter antimatter fluctuations, Monograph, LAP Lambert (2011)

Chapter 4

Data samples selection and composition

In this chapter we give an outline of the trigger strategies used to collect the data samples, and describe the criteria employed to reconstruct and select B^+, B^0, and B_s signal candidates in multiple decay modes. The data sample was recorded with the CDF detector in the period from early 2002 to early 2006. This amounts to an integrated luminosity of approximately $1\,\mathrm{fb}^{-1}$, after imposed quality requirements, *i.e.* taken with the full detector systems properly functioning. The accurate understanding of the selected samples will benefit from Monte Carlo simulation of the involved signals, including detector and trigger selection effects. Such Monte Carlo samples will be employed in the process of signal optimization, as well as to assess the samples composition.

The following B meson decay modes are reconstructed,

- $B^+ \to J/\psi K^+$,
  $B^+ \to \bar{D}^0\pi^+$, $B^+ \to \bar{D}^0\pi^+\pi^-\pi^+$,
  $B^+ \to \bar{D^0}l^+\nu$,

- $B^0 \to J/\psi K^{*0}$,
  $B^0 \to D^-\pi^+$, $B^0 \to D^-\pi^+\pi^-\pi^+$, $B^0 \to D^{*-}\pi^+$, $B^0 \to D^{*-}\pi^+\pi^-\pi^+$,
  $B^0 \to D^-l^+\nu$, $B^0 \to D^{*-}l^+\nu$,

- $B_s \to D_s^-\pi^+$, $B_s \to D_s^-\pi^+\pi^-\pi^+$,
  $B_s \to D_s^-l^+\nu$,

where the lepton l stands for electron (e) or muon (μ), and the involved charm and strange mesons are reconstructed in the following channels,

- $D^- \to K^+\pi^-\pi^-$,

- $D^0 \to K^-\pi^+$, $D^0 \to K^-\pi^+\pi^-\pi^+$,
- $D^{*-} \to \bar{D}^0\pi^-$,
- $D_s^- \to \phi\pi^-$, $D_s^- \to K^{*0}K^-$, $D_s^- \to \pi^+\pi^-\pi^-$,
- $\phi \to K^+K^-$,
- $K^{*0} \to K^+\pi^-$,
- $J/\psi \to \mu^+\mu^-$.

Charge-conjugated states are implicitly assumed throughout the text. The full list of decay chains is shown explicitly in Table 4.1.

The B meson decays studied fall into two categories: fully reconstructed and partially reconstructed. The former category corresponds to the $B \to J/\psi K$ and $B \to D\pi(\pi\pi)$ modes. The latter class is realized by the $B \to Dl\nu$ decays, where the neutrino and possibly other decay products are missed. The resulting samples will be sometimes also referred to as *hadronic* and as *semileptonic*, respectively.

The semileptonic modes provide relatively larger samples of B mesons. The full reconstruction which characterizes the hadronic modes, however, is translated in a more accurate determination of the candidates' proper decay time, which will reveal an important effect especially in the analysis of B_s oscillations.

4.1 Trigger requirements

The data are acquired through trigger requirements, imposed *online*, *i.e.* in real-time, by the data acquisition system.

Muons allow for a clean identification, and are used to collect samples of J/ψ mesons, partially fed by B decays. The possibility of triggering on events displaced from the interaction point, by exploring the long lifetime of b-hadrons, is made possible for the first time at a hadron detector by the CDF Silicon Vertex Trigger (SVT) processor. Such criteria for selecting events formed of displaced tracks are used in the other two of the three trigger paths employed, which are described next.

Di-muon trigger

The B decays involving a J/ψ meson in the final state are selected by identifying a pair of muon candidates, with opposite charges, and a mass, $M_{\mu\mu}$, close to the J/ψ nominal mass. The specific requirements are summarized by the following:

A. Level 1

- two XFT tracks with opposite charge,
- each track is matched with two muon stubs,
- each CMU(CMX) muon has $p_T^{\mathrm{XFT}} > 1.5\,(2.2)$ GeV/c,
- $\Delta\phi_6(\mathrm{CMU},\mathrm{CMU}) < 135°$, no cut in $\Delta\phi_6(\mathrm{CMU},\mathrm{CMX})$,

B. Level 3

- $2.7 < M_{\mu\mu} < 4$ GeV/c^2,

where p_T^{XFT} is the track transverse momentum as measured by XFT, and $\Delta\phi_6$ is the opening angle at the COT superlayer 6.

Two displaced-tracks trigger

The trigger criteria include the requirement of two displaced tracks forming a displaced vertex. The specific requirements are summarized as follows:

A. Level 1

- two XFT tracks with opposite charges,
- each track has $p_T^{\mathrm{XFT}} > 2.04$ GeV/c,
- $\sum p_T^{\mathrm{XFT}} > 5.5$ GeV/c,
- $0° < \Delta\phi_6 < 135°$,

B. Level 2

- for each track, 100 μm $\leq |d_0^{\mathrm{SVT}}| \leq 1$ mm,
- each track has $p_T^{\mathrm{SVT}} > 2$ GeV/c,
- $\sum p_T^{\mathrm{SVT}} > 5.5$ GeV/c,
- $2° < \Delta\phi_0 < 90°$,

C. Level 3

- $|\Delta z_0| < 5$ cm,
- two-track vertex $L_{xy} > 200$ μm,

where d_0^{SVT} is the impact parameter as measured in the SVT, Δz_0 is the distance between the two tracks along the beam axis, and L_{xy} is the distance in the transverse plane of the two-track vertex with respect to the primary vertex.

Lepton and displaced-track trigger

The strategy is to identify semileptonic B decays by requiring the presence of a lepton with large transverse momentum together with a displaced track. The specific requirements are summarized as follows:

A. Level 1

for the lepton:

- track with $p_T^{\mathrm{XFT}} > 4$ GeV/c,
- $E_T > 4$ GeV, $E_{\mathrm{HAD}}/E_{\mathrm{EM}} < 0.125$, or

  track with stubs in both CMU and CMP,

for the displaced-track:

- $p_T^{\mathrm{XFT}} > 4.09$ GeV/c,
- $0^\circ < \Delta\phi_6 < 100^\circ$,

B. Level 2

for the displaced-track:

- 120 μm $\leq |d_0^{\mathrm{SVT}}| \leq 1$ mm,
- $p_T^{\mathrm{SVT}} > 2$ GeV/c,

C. Level 3

for the lepton displaced-track pair:

- $2^\circ < \Delta\phi < 90^\circ$,
- mass < 5 GeV/c^2 .

These trigger samples contain large numbers of semileptonic B meson decays. These are primarily used in an inclusive fashion for the study and optimization of opposite-side flavor tagging methods. Semi-exclusive semileptonic signals may additionally be extracted, although this is not done in the context of this dissertation.

4.2 Event reconstruction

The data samples collected according to the specified trigger criteria undergo further manipulations, which lead to precise and complete reconstruction of physics objects suitable for data analysis. During the production stage more accurate detector calibration and alignment information is available than was used during data taking. Tracks, which are reconstructed at CDF using several algorithms [50], form the basis for the reconstruction of B meson decay candidates.

4.2.1 Track selection and preparation

Tracks are used to reconstruct decaying particles' vertices, the resolution of which is a determining factor for the measurements to be performed. This renders the use of well-measured tracks further imperative. It is therefore important to ensure that tracks which are used for reconstructing candidates meet standards for good quality in each of the detector subsystems. Furthermore, all tracks are refit in order to achieve improved determination of track parameters and associated uncertainties.

Mis-alignments together with hits caused by noise in the tracking system produce fake and mis-measured tracks in the events. The number of such occurrences is decreased by requiring for the track a minimum number of hits in the drift chamber and silicon detector. Specifically these track-quality criteria involve requiring at least 10 axial and 10 stereo COT hits, 3 SVX hits, and a minimum track momentum of 350 MeV/c.

Selected tracks are required to have a COT parent, with a physical covariance matrix, and a helix fit attached. The ascribed uncertainties to the COT hit positions, which do not take into account the effect of multiple scattering in the material of the COT system, determine an underestimation of the track parameters returned by the track fit. In order to correct for COT resolution effects which are not well understood, the covariance matrix of the COT track is rescaled with the following empirical scaling factors [51] (with p_T in GeV/c):

$$\begin{aligned}
s(\lambda) &= \sqrt{1 + p_\lambda (1+\lambda^2)^{1.5}/p_T^2} \quad \text{with} \quad p_\lambda = 0.58; \\
s(C) &= \sqrt{1 + p_C/p_T^2} \quad \text{with} \quad p_C = 5.33; \\
s(z_0) &= \sqrt{1 + p_{z_0} (1+\lambda^2)^{1.5}/p_T^2} \quad \text{with} \quad p_{z_0} = 0.653; \\
s(d_0) &= \sqrt{1 + p_{d_0}/p_T^2} \quad \text{with} \quad p_{d_0} = 3.01; \\
s(\phi_0) &= \sqrt{1 + p_{\phi_0}/p_T^2} \quad \text{with} \quad p_{\phi_0} = 3.7.
\end{aligned}$$

Here $\lambda = \cot\theta$, with θ being the polar angle of the track; the signed curvature of the track

is referred to as C, with the magnitude given by the inverse of the trajectory diameter; the parameters z_0, ϕ_0, and d_0 are the coordinates of the point of closest approach to the beamline. The factors are applied to the covariance matrix as $c_{ij}^{\text{new}} = s_i s_j c_{ij}^{\text{old}}$, where the indices i and j represent the various helix parameters.

The rescaled track is finally refit with the addition of the silicon hits. For properly positioning the silicon hits an alignement table is used. When the data gets officially reconstructed the final alignement table is usually not yet available. Therefore we use here the most up-to-date version, for optimal resolutions. If available, hits on the Layer 00 silicon subsystem are also included in the track refit procedure. The inclusion of the additional constraints provided by this innermost silicon detector system on the particle tracks results in improvements in vertexing resolution. This translates eventually in $\sim 10\%$ improvements in decay length resolution. The refitting of the track takes into account corrections to energy loss in the detector material for kaon, pion, electron or muon hypotheses according to the requested species. The description of the passive material settings is based on [52].

The location of the primary interaction vertex of the event, where the b hadron was produced, needs to be determined. A good approximation of its location is the beam spot. We use an improved determination which is provided by an iteractive procedure [53]. A set of loosely selected tracks is combined to form a vertex, and at each fit iteration the track with worst χ^2 is eliminated. The procedure is repeated until no track has a χ^2 larger than a maximum allowed value. The tracks belonging to the reconstructed B meson decay candidate are excluded from the procedure.

4.2.2 Pre-selection and BStntuple

Trigger confirmation

The confirmation of the trigger requirements is important given that there are differences between the online and offline reconstruction tracks. For example, the SVT fit does not use the exact same algorithm and information which characterizes the tracks obtained from production. Connecting these production tracks with the online trigger information avoids considering so-called volunteer candidates. These are such candidates for which not all trigger tracks correspond to B decay products. These may arise, for example, when an SVT trigger track is provided by a fake XFT track, which got several accidental hits assigned and has thus high probability to have a large impact parameter; or when the lepton or a SVT track belong in fact to the other B hadron in the event.

In order to ensure that we have a displaced SVT track a matching is performed between the production and SVT tracks. The SVT matching algorithm compares the curvature and

the ϕ of the two tracks, and requires for the quadratic sum of the normalized distance in the two parameters between the tracks a maximum default value. Differences in ϕ, for example, may also to some extent have origin in the fact that different silicon alignments are used for SVT and offline reconstruction. Only SVT tracks which have an SVT χ^2 larger than 25 are considered. To promote a production level track to being matched to an online SVT trigger track we further require that the SVT measurements of p_T and d_0 comply with $p_T > 2$ GeV/c and 0.012 cm $< |d_0| <$ 0.100 cm.

General pre-selection

Candidates for each particle decay tree are constructed from the bottom up. For example, in the case of $B \to l^+ D_s^- X(D_s^- \to \phi\pi^-, \phi \to K^+K^-)$ we start with a $\phi \to K^+K^-$ decay, which in the next step is used to make candidates for the $D_s^- \to \phi\pi^-$ decay and finally those are used to form $B \to l^+ D_s^- X$ decays. In each step the candidates are subjected to a set of selection requirements which is chosen to quickly reject uninteresting candidates. Charge correlations among the tracks are applied first. Candidates with duplicate tracks are removed. The trigger is confirmed when applicable: for $D_{(s)}$ candidates one matched SVT trigger track is required in the case of semileptonic modes; for the hadronic B decays, two of the tracks forming the B candidate are required to be matched to an SVT trigger track pair, and these may belong to any child of the B meson: D_s^-, D^-, D^0, D^{*-}, $\pi(\pi\pi)$ or any combination thereof.

The raw mass is calculated based on the fully corrected track momentum and candidates are only accepted within loose mass windows. A vertex fit [44] is performed to the decay topology, and the resulting χ^2 in the r-ϕ plane, $\chi^2_{r\phi}$, the fitted mass, and the two-dimensional decay length, L_{xy}, are used to reject candidates. Cuts are only applied if tighter cuts are used later in the analysis.

BStntuple

We have implemented a framework, here referred to as the `BStntuple` [54], for efficiently storing and accessing the selected data information which forms the B mesons candidates. It shares the basic structure of the standard `stntuple` [55], which itself constitutes, in practice, a more sophisticated `ntuple` together with a set of convenient tools; its format shares features of both micro-DST and `Root` files. It contains structures to hold the reconstructed candidates information (stable and decaying objects) as well as taggers' information (decision, raw dilution), and particle identification information (TOF, dE/dx, muon and electron quantities). The actual data blocks correspond to instances of these classes for specific de-

cay modes, which are implemented by cloning prototype modules appropriate for the decay topology. This has revealed to be an efficient and uniforming framework, in terms of both CPU usage time and procedure sharing, which has facilitated candidate reconstruction and the ntupling process for the various decays and data samples employed in the analysis.

4.2.3 Selection optimization

In deciding on the requirements for selecting B candidates which will form our samples the goal is to optimize the samples' effective statistical significance in view of the measurements which are to be performed.

The significance of a sample for a mixing analysis is estimated via (11.17), and in principle this full quantity should be considered as optimization criteria. This includes a quantification of the signal yield and purity, through the variable

$$\frac{N_S}{\sqrt{N_S + N_B}}\,, \tag{4.1}$$

where N_S and N_B are the number of selected signal and background events, respectively. This is the main criterion for sample selection optimization which has been employed.

In addition, it is possible to appropriately weight signal events according to their proper time resolution, by including the following multiplicative term

$$\frac{1}{N_S}\sum_{i=1}^{N_S} e^{-(w\sigma_i)^2}\,, \tag{4.2}$$

where σ_i is the event resolution, and w stands for a value in the vicinity of the mixing frequency being probed. These additional effects are relevant mostly for the study of flavor oscillations in samples of B_s mesons. Such a correction to the optimization criteria has in fact been implemented for the semileptonic B_s samples, while no appreciable requirement modifications have been induced. Contributions from flavor tagging, which would depend on algorithm specifics, to the effective significance (11.17), are not considered in the selection process.

The optimization procedure is performed after a set of variables with appropriate discriminating power between signal and background is found. For each set of cut values of the variables being optimized, the quantity to be maximized, which we have addressed above, is evaluated. The effect of the selection requirements on the background is evaluated using the data sample itself, while for signal Monte Carlo simulated events are employed, in order to ensure that cuts are not biased. The number of background events is estimated by applying the selection requirements to a sample of the data where no signal events are present ("sideband"). The mass of the sideband events is fit with a linear ($J/\psi K$ and Dl modes) or an

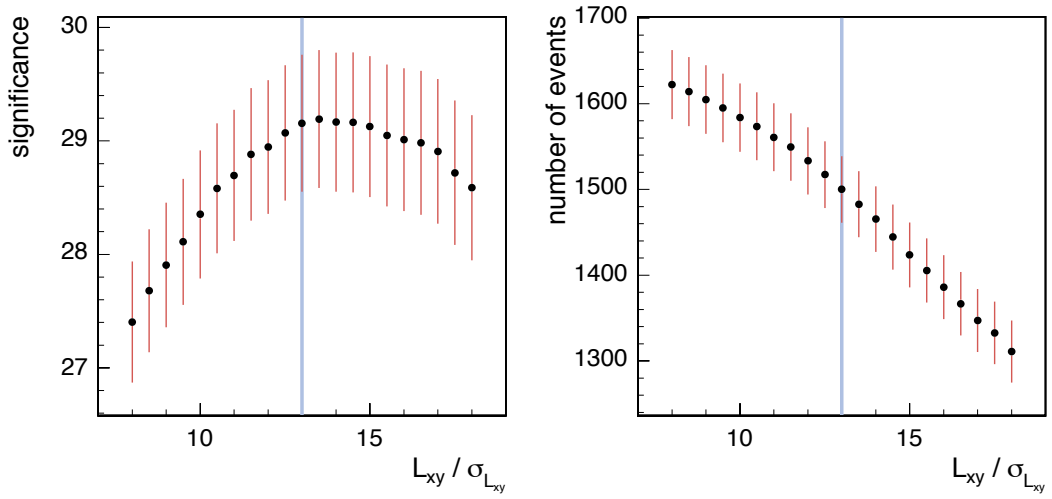

Figure 4.1: Illustration of selection optimization procedure applied to $L_{xy}/\sigma_{L_{xy}}$: significance (left) and efficiency (right).

exponential ($D\pi(\pi\pi)$ modes) model, which is extrapolated to and integrated in the signal region. The number of signal events is determined from the Monte Carlo sample, after this is rescaled to the number of events found in the mass peak in data before optimization.

The procedure is iterative. At a given iteration, a set of best values is found for the set of variables being optimized – each variable is varied at a time while all others are kept fixed, and that value which maximizes the significance is found. The procedure is repeated until convergence is observed. The optimization process is illustrated in Figure 4.1 for the cut $L_{xy}/\sigma_{L_{xy}}$. Besides the significance being maximized, shown on the left, the other variable which is monitored in the process is the analysis efficiency, shown on the right hand side figure. When a set of points is found with similar significance, the point with highest efficiency is chosen.

4.2.4 Reconstruction of B decays

Variables

Several variables have been identified which are useful for reducing the combinatorial background levels of our samples. A selection based on these variables is optimized, as described above, for each of the decay channels reconstructed, in order to achieve maximal signal significance.

B mesons are relatively long-lived particles thus producing measurable decay distances

in the detector. That is, the B decay vertex tends to be significantly displaced from the primary interaction point. Additionally, D mesons have themselves a finite (though somewhat smaller) lifetime as well, making their decay vertex displaced with respect to that of the parent B. The selection criteria attempt therefore to select the resulting decay topologies, which are furthermore kinematically consistent with the particle hypotheses forming the studied decay trees.

Various variables are available for implementing selection criteria allowing to statistically identify the signal decays with such characteristics from backgrounds produced by other, random track combinations. A list of some of the most common follows. The quality of fits to tracks forming vertices of B and D meson candidates is given by the $\chi^2_{r\phi}$ in the transverse r-ϕ plane or the three dimensional vertex fit probability. The transverse distance, L_{xy}, of B and D meson decay vertices relative to the primary interaction vertex, or the transverse decay distance of the D meson relative to the B meson, $L_{xy}(B \leftarrow D)$, as well as the transverse decay distance uncertainty, $\sigma_{L_{xy}}$, are used to identify displaced objects. The transverse momenta, p_T, of particle candidates are widely useful. So are the masses associated to vertices, which are provided by the vertex fit, and to track systems such as that of a D-lepton pairs m_{Dl}, and mass differences such as $m(D^*) - m(D^0)$, which also provide powerful criteria.

Building blocks

The $J/\psi \to \mu^+\mu^-$ decay candidates are formed from pairs of trigger muons and are required to have a mass within ± 80 MeV/c^2 of the world average J/ψ mass.

The $K^{*0} \to K^+\pi^-$ candidates are reconstructed from track pair combinations that fit into a common vertex. They are required to fall into a $\pm(50-60)$ MeV/c^2 mass window about the K^{*0} world average mass. Due to the broadness of the K^{*0} resonance and the absence of particle identification in the selection analysis, it is not uncommon for a track pair to have both possible mass assignments $K^+\pi^-$ and π^+K^- found in the allowed mass region for the K^{*0}. No attempt is made to discriminate between the true and the swapped K^{*0} candidates, and all combinations are accepted. While this ambiguity is removed in the case of the $D_s^- \to K^{*0}K^-$ decay, through charge correlation, the fraction of signal $B^0 \to J/\psi K^{*0}$ candidates formed of the swapped mass assignment is estimated in Section 4.3 from Monte Carlo predictions.

The ϕ meson candidates are reconstructed from a pair of oppositely charged kaons, which is required to have a mass consistent with the ϕ nominal world average mass value, in a window of ± 12 MeV/c^2.

The decays of the charmed mesons $D^0 \to K^-\pi^+$, $D^0 \to K^-\pi^+\pi^-\pi^+$ and $D^+ \to K^-\pi^+\pi^+$ are reconstructed by combining two, four and three tracks, respectively, and applying the

standard vertex fit. A loose mass cut is applied to the D^0 and D^+ candidates by requiring that they be in the range of $(1.77, 1.97)$ GeV/c^2. The cuts for the D vertex quality vary depending on the decay channel of the parent B. In the semileptonic samples the D^0 meson is reconstructed in the lower multiplicity mode only.

The $D^{*-} \to \bar{D}^0\pi^-$ meson candidates are reconstructed by combining the D^0 with appropriately charged pion candidate tracks. Both $D^0 \to K^-\pi^+$ and $D^0 \to K^-\pi^+\pi^-\pi^+$ collections are used for the D^{*-} reconstruction in hadronic samples, while only the former is employed in the semileptonic samples. The reconstructed mass of the D^{*-} is required to be within ± 80 MeV/c^2 of the PDG value. Subsequently, a cut on $\Delta M_{D^*} \equiv m_{D^*} - m_{D^0}$ is applied. In the mass difference calculation, the fitted masses m_{D^*} and m_{D^0} are used; the track 4-momenta of the D^0 daughters are taken from the stand-alone D^0 mass fit without the D^0 mass constraint. The momentum of the slow pion from D^* is taken from the fit of the D^*; for D^*l decays, this momentum should have a magnitude of at least 0.4 GeV/c.

In any triple-pion decay mode such as $B^0 \to D^-\pi^+\pi^-\pi^+$ or $B^0 \to D^{*-}\pi^+\pi^-\pi^+$, there are three pion tracks which come directly from the B decay vertex. Triple pion combinations are formed from all eligible tracks in an event and are fitted to have a common origin using the standard vertex fit. Vertex quality requirements are applied on these vertices. In addition, an invariant mass cut allows for significant reduction of otherwise overwhelming combinatorics from random tracks in the event. For a triple pion combination to come from a B meson in $B \to D\pi\pi\pi$ decay, it has to have a mass no larger than m_B-m_D. The chosen cuts on the $\pi\pi\pi$ vertex quality and mass are shown in Table 4.3.

The D_s meson candidates are reconstructed in three final states: $\phi\pi$, K^*K, and $K\pi\pi$. The requirement on the invariant mass corresponds to the range of $(1.90, 2.04)$ GeV/c^2. The possibility of having background coming from reflections under this D_s mass region has been investigated, by modifying the mass assignment of the particles and checking the different mass distributions. The $D_s \to K^*K$ case has a substantial reflection from $D \to K^*\pi$, $K^* \to K\pi$ and $D \to K\pi\pi$ (non-resonant) decays. The requirement $|m(K\pi\pi) - m^{D^+}_{PDG}| < 20-24$ MeV/c^2 while having a 60% efficiency for signal reduces that background to negligible levels. In the $D_s \to \pi\pi\pi$ channel there is a large contribution coming from $D^* \to D^0\pi$, $D^0 \to K\pi\pi$ decays; requiring $m(K\pi\pi) - m(K\pi) > 150$ MeV/c^2 was shown to reduce to very low levels the D^* background, with essentially no loss of signal candidates. In the case of $D_s \to \phi\pi$, due to the narrow ϕ mass window, no substantial reflections are observed. The cuts used for reconstructing D_s in the semileptonic samples are shown in Table 4.5. The helicity angle ψ is calculated in the ϕ or K^{*0} rest frame, and is defined as the angle between the momentum of the D_s candidate and the direction of the two decay products, e.g. $\phi \to K^+K^-$.

For selecting the lepton tracks from B decays we use lepton identification likelihood techniques, which combine related variables from various detector components. These coincide with those developed for the soft lepton taggers [56, 57]. The transverse momentum threshold for the lepton identification has been set to $p_T \geq 1.5$ GeV/c. For electrons, the likelihood is required to be larger than 0.9. In case of muon identification the cut value depends on the muon system: 0.05 (CMUP), 0.50 (CMU,CMP,CMX), and 0.70 (IMU).

B meson reconstruction

B meson candidates are formed from the building blocks constructed above. Vertex fits are applied to the resulting combinations, according to the reconstructed decay channels. The masses of the J/ψ, D^0, D^-, D_s^- meson candidates are constrained in these fits to the corresponding world average mass values. No pointing constraints are imposed for either J/ψ, D or B mesons.

The decay candidates $B^+ \to J/\psi K^+$ and $B^0 \to J/\psi K^{*0}$ are formed by pairing the J/ψ candidates with charged tracks and with K^{*0}. The vertex fit is performed on the three and four track combinations for the B^+ and B^0 candidates, respectively. The kinematic and quality cuts applied to the resulting candidates are listed in Table 4.2.

The list of $B \to D^{(*)}\pi(\pi\pi)$ modes is found in Table 4.1. For each newly formed candidate, the full vertex fit is performed. A number of (optimized) kinematic and vertex quality cuts are then applied to reduce the combinatorial background; these are specified in Table 4.3.

The reconstructed hadronic B_s channels include $B_s \to D_s^-\pi^+$ and $B_s \to D_s^-\pi^+\pi^-\pi^+$ with D_s decaying through three different channels: $D_s^- \to \phi\pi^-$, $D_s^- \to K^{*0}K^-$ and $D_s^- \to \pi^-\pi^+\pi^-$. The mode $B_s \to D_s^-\pi^+\pi^-\pi^+$, $D_s^- \to \pi^-\pi^+\pi^-$ has not been considered due to the large amount of combinatorial background. The full list of selection cuts is shown in Table 4.4.

The collection of partially reconstructed semileptonic B^+, B^0, and B_s decays is listed in Table 4.1. Each candidate is obtained by combining a lepton and a D meson, on which a full vertex fit is performed. The optimization of kinematic and vertex quality cuts has been performed for the six Dl nominal modes individually. We point out that the requirement on the invariant mass of the lepton and the D meson, m_{Dl}, has revealed to be rather powerful in rejecting background, especially the denominated *fakes* background which is of non-combinatorial type as will be analyzed in the following section. The selection criteria are summarized in Table 4.5 for all Dl samples.

4.3 Samples composition

Samples of both fully and partially reconstructed B meson candidates are studied in this dissertation. In this section we assess the yields and study the various sources and type of candidates which contribute to their composition.

4.3.1 Sub-samples classification

The signal yields of the fully reconstructed decay samples are summarized in Table 4.6.

As it was mentioned in Section 4.2.2, it is required that the production tracks matched to the two trigger tracks be among the B daughters. In the case of semileptonic samples, if the lepton corresponds to one such track the event is said to be of the "*B trigger*" type, otherwise both trigger tracks are matched to the D daughters and the event is thus denoted of the "*D trigger*" type. For each of the Dl decay samples – D^*l, D^0l, D^+l, and D_s^-l – the following event sub-categories are considered: μ and e events, B and D trigger events. As these sub-samples have relatively different characteristics, such as background fractions and decay-length distributions, the analysis takes into account this classification with the aim of gaining in overall signal significance. The initial six semileptonic decay samples become therefore arranged in a total of 24 sub-samples, according to this further classification. The yields for these sub-samples are provided in Table 4.7.

The following ct regions are allowed for the Dl samples,

$D^{(*)}$:	$ct \in [50, \infty)\ \mu$m,
$lD_s^-[\phi\pi^-]$, B trigger:	$ct \in [50, \infty)\ \mu$m,
$lD_s^-[\phi\pi^-]$, D trigger:	$ct \in [100, \infty)\ \mu$m,
$lD_s^-[K^{*0}K^-, \pi^+\pi^-\pi^-]$, B and D triggers:	$ct \in [100, \infty)\ \mu$m.

4.3.2 Fully reconstructed B samples

The reconstructed nominal signal decays in the $J/\psi K$ samples are $B^+ \to J/\psi K^+$ and $B^0 \to J/\psi K^{*0}$. In order to identify misreconstructed candidates in the samples, the signal selection criteria are applied to Monte Carlo samples of b-hadron $\to J/\psi X$ decays [58, 59]. Figure 4.2 shows the mass distributions obtained from various contributing channels in such inclusive Monte Carlo samples, reconstructed as $B^+ \to J/\psi K^+$ and $B^0 \to J/\psi K^{*0}$.

The fitting mass region for these samples is $(5.17, 5.39)$ GeV/c^2. This is chosen to avoid sources of partially reconstructed decays which are present for masses below about 5.17 GeV/c^2. Two predominant contributions from misreconstructed decays remain, arising from incorrect identification of kaons and pions.

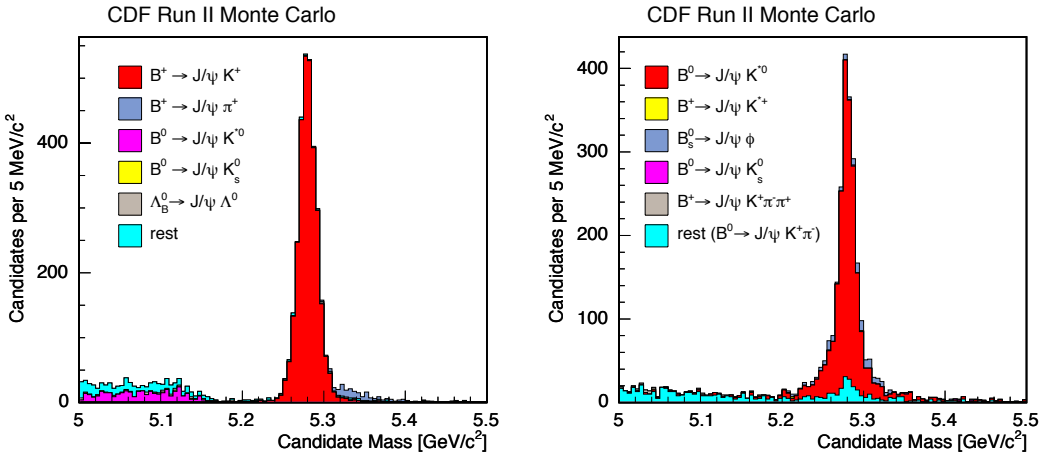

Figure 4.2: Monte Carlo mass distributions of b-hadron $\to J/\psi X$ decays, reconstructed as $B^+ \to J/\psi K^+$ (left), and $B^0 \to J/\psi K^{*0}(K^+\pi^-)$ (right).

The Cabibbo-suppressed $B^+ \to J/\psi\pi^+$ decays, with the pion misidentified as a kaon, have a reconstructed mass slightly above the nominal B^+ mass. This contribution amounts to a fraction of candidates relative to the nominal decay which is reported in Table 4.8.

In the case of the $B^0 \to J/\psi K^{*0}$ mode, a self-reflection arises from $K^{*0} \to K^+\pi^-$ decays which are reconstructed with wrong (*swapped*) pion and kaon mass assignments to the two forming tracks. The relative contribution of these swapped candidates is extracted from a sample of signal Monte Carlo to which the selection criteria are applied. We observe that the mass distributions for both the correctly reconstructed candidates and those formed of swapped K^{*0} have a general Gaussian shape, as shown in Figure 4.3. These are characterized by widths of 10.5 and 25.5 MeV/c^2, with that of the swapped component being broader; the relative fraction is reported in Table 4.8.

The list of fully reconstructed $B \to D\pi(\pi\pi)$ decays is included in Table 4.1. The reconstructed mass spectra for these modes show various satellite structures. Their source is investigated by identifying the contributions in Monte Carlo simulation from the involved decays when reconstructed as the nominal signal modes [60]. Figures 4.4 and 4.5 illustrate these for B^+, B^0, and B_s decays, in a wide mass range.

A narrow fitting mass range is chosen which, as it was the case for the $J/\psi K$ samples, excludes, or substantially reduces, several of the structures appearing in the low mass region relative to that of the nominal signal. The upper limit of the mass interval is chosen at 5.6 GeV/c^2, while the lower limit is set at 5.2 GeV/c^2 for B^+ and B^0 decays, and at 5.3 GeV/c^2 for the B_s modes.

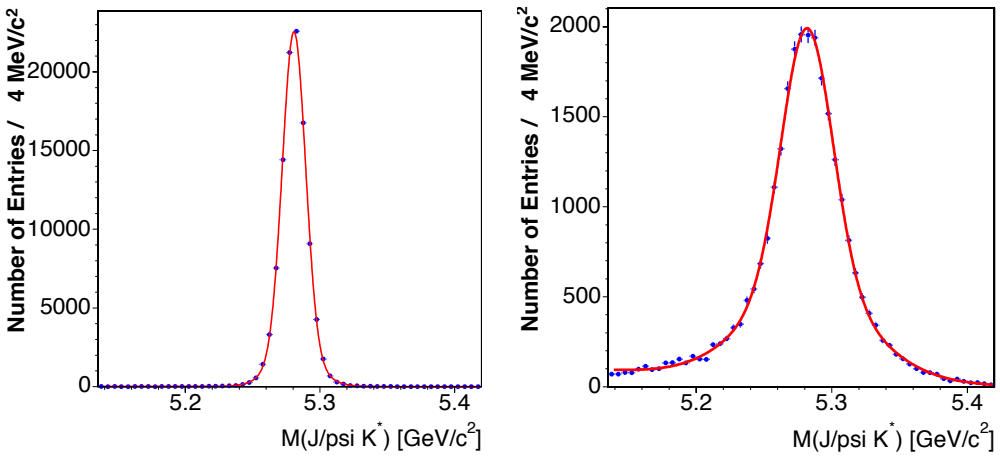

Figure 4.3: Mass distribution for $B^0 \to J/\psi K^{*0}$ candidates reconstructed in the signal MC sample when the K^* is reconstructed correctly (left), and when it is mis-reconstructed with swapped K and π assumptions (right).

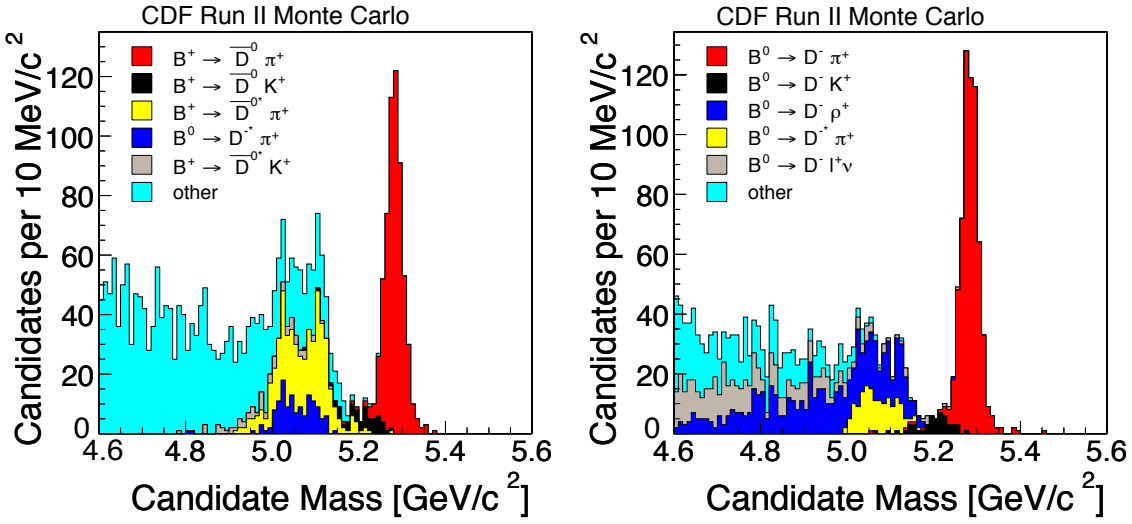

Figure 4.4: Monte Carlo mass distributions of b-hadron $\to DX$ decays, reconstructed as $B^+ \to \bar{D}^0\pi^+$ ($\bar{D}^0 \to K^+\pi^-$) (left), and $B^0 \to D^-\pi^+$ ($D^- \to K^+\pi^-\pi^-$) (right).

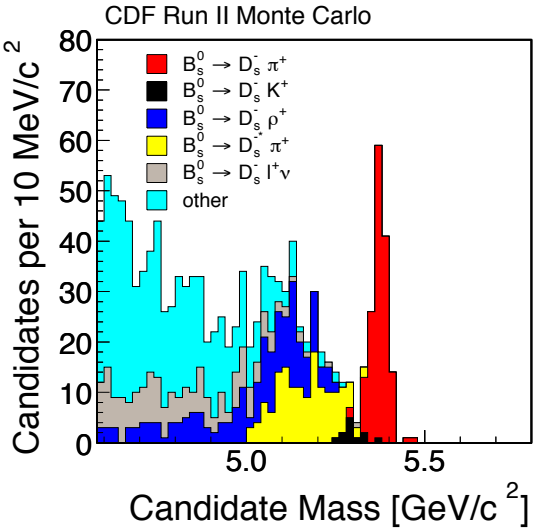

Figure 4.5: Monte Carlo mass distributions of b-hadron $\to D_s X$ decays, reconstructed as $B_s \to D_s^- \pi^+$ ($D_s^- \to \phi\pi^-$).

Despite having selected a restricted mass range, there is still some contamination which leaks into this narrower fitting mass region. The contribution of such partial reconstructed decays is extrapolated to the narrower mass region from a fit to the data performed in the extended mass spectrum. The numerical results for their contributions relative to the nominal signals are summarized in Table 4.9. These extended fits are in addition most relevant for determining the combinatorial background behavior. The details on the wide mass range fits are addressed further below.

The Cabibbo-suppressed decays $B \to D^{(*)}K(\pi\pi)$, where the kaon track is misassigned the pion mass, appear as small contributions underneath the main mass peaks in the hadronic samples. The shape and the relative amount of these components can be predicted from Monte Carlo simulation, where the branching fraction of the Cabibbo-suppressed mode is set to the expected amount based on the Cabibbo angle relative to the Cabibbo-favored modes. These contributions are of the level of about 6% relative to the nominal signals. The fractions evaluated for each mode are specified in Table 4.10, and the mass shape is illustrated for the main hadronic B_s mode in Figure 4.6.

There is some amount of cross-talk among the various hadronic modes. For example, the decay channels $B_s \to D_s^- \pi^+$ ($D_s^- \to K^+K^-\pi^-$) may be reconstructed as $B^0 \to D^-\pi^+$ ($D^- \to K^+\pi^-\pi^-$) in case the kaon is misidentified as a pion. The inverse also occurs, when $B^0 \to D^-\pi^+$ ($D^- \to K^+\pi^-\pi^-$) decays are misreconstructed in one of the $B_s \to D_s^-\pi^+$ modes. There are additional background sources coming from misreconstructed $\Lambda_b^0 \to \Lambda_c^+\pi^-$

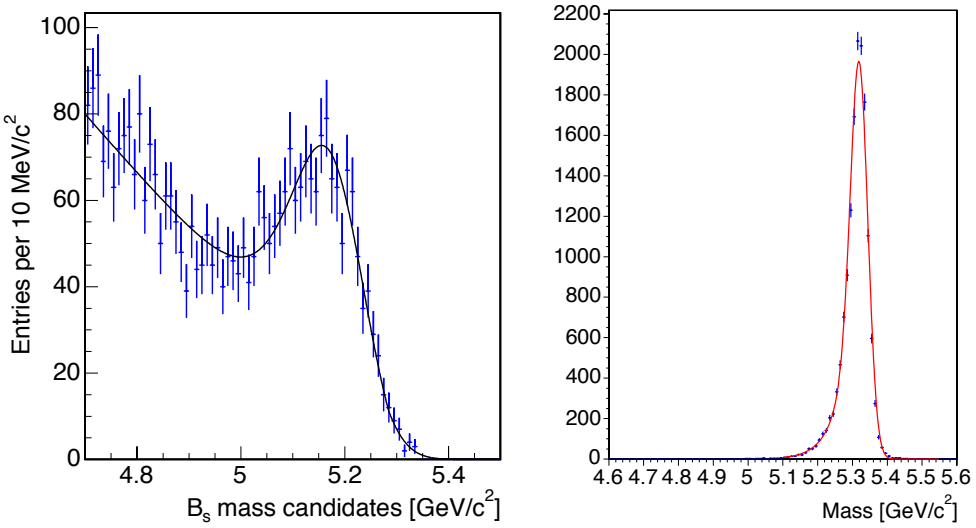

Figure 4.6: Mass templates for partially reconstructed (left) and Cabibbo-suppressed (right) background decays, illustrated with the $B_s \to D_s^- \pi^+$ ($D_s^- \to \phi\pi^-$) channel.

($\Lambda_c^+ \to p^+K^-\pi^+$) decays, where the proton is misidentified with a kaon or a pion. The contributions of such decays relative to the nominal signals are obtained from the ratio of the relevant branching fractions, and trigger and reconstruction efficiencies evaluated from Monte Carlo simulation. These fractions are summarized for all B_s channels in Tables 4.11 and 4.12.

Wide range mass fits

In order to gain understanding of background components in the hadronic $D\pi(\pi\pi)$ samples, we perform a fit to the mass distribution of the data in an extended mass range. Specifically, the selected wider mass intervals are $(4.4, 7.6)$ and $(4.6, 5.6)$ GeV/c^2 for the B^+ and B^0 and the B_s samples, respectively.

The region to the left of the nominal signal peak in the mass distribution contains various structures. The corresponding sources are identified from Monte Carlo simulation, as illustrated in Figures 4.4 and 4.5. These include partially reconstructed $B_{(s)} \to D_{(s)}\pi X$ and $B_{(s)} \to D_{(s)}l\nu$ decays. In the latter case the lepton is misreconstructed as a pion, while the former class of candidates includes $B_{(s)} \to D_{(s)}\rho$ decays, and $B_{(s)} \to D^*_{(s)}\pi$ decays, with the $D^*_{(s)}$ decaying to $D_{(s)}\gamma$ and to $D_{(s)}\pi^0$ and the γ and π^0 not being detected.

The shape of the templates describing the background constituted by partially reconstructed decays is modeled using inclusive B Monte Carlo samples, $b \to D_{(s)}X$. The

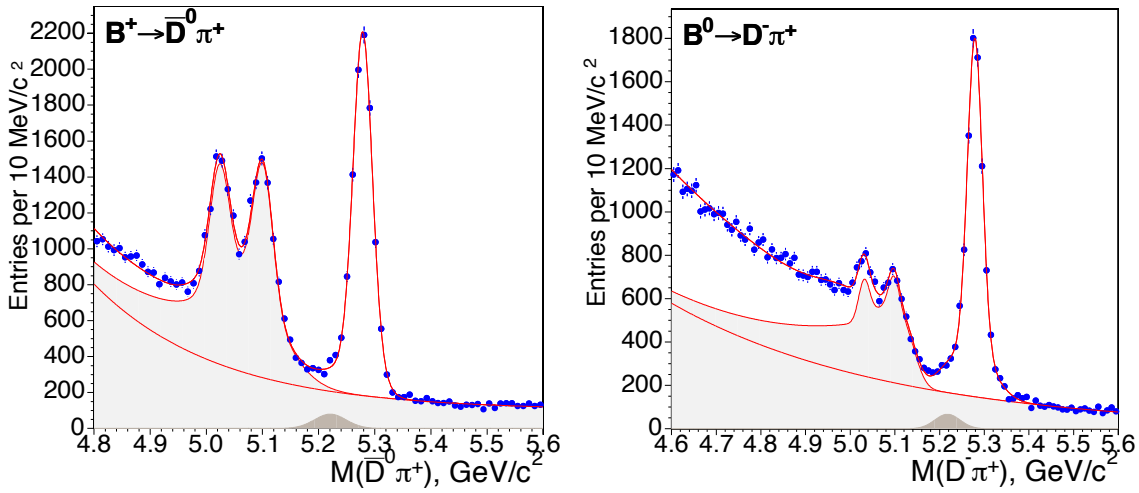

Figure 4.7: Wide range mass fits for $B^+ \to \bar{D}^0\pi^+$ (left) and $B^0 \to D^-\pi^+$ (right) candidates.

$B_{(s)} \to D_{(s)}\rho, D^*_{(s)}\pi$ decays, and those which include leptons in the final state or in which more than a pion is lost are treated by separate templates. These correspond to a smeared Gaussian model, and a linear shape with a cut-off, respectively. In Figure 4.6 the combined templates are illustrated for the main B_s decay mode. The relative normalizations between the two template models is allowed to float in the fit.

The fully reconstructed backgrounds have already been addressed. These tend to have shapes of bumps not much wider than the signal peak, and place themselves in the vicinity of it. As it was observed before, the description of these components needed to be inferred from Monte Carlo simulation, which is imposed in the fit.

The contribution of the Cabibbo-suppressed decays, as it was also addressed, is predicted from Monte Carlo simulation. The relative fractions are summarized in Table 4.10. In the fit to the data the shape of this component is also fixed from simulation; its width is dominated by kinematic smearing, rather than detector resolution, due to mass mis-assignment. The template is illustrated in Figure 4.6.

The wide range mass fit projections are shown in Figures 4.7 and 4.8 for the main $\bar{D}^0\pi^+$, $D^-\pi^+$, $D_s^-\pi^+$, and $D_s^-\pi^+\pi^-\pi^+$ channels. The shape parameters and normalization of the combinatorial background component float free in the fits.

4.3.3 Partially reconstructed B samples

The Dl candidates are formed of a combination of a lepton and D meson pair consistent with having originated from a B meson decay. The lepton l is identified as either an electron or

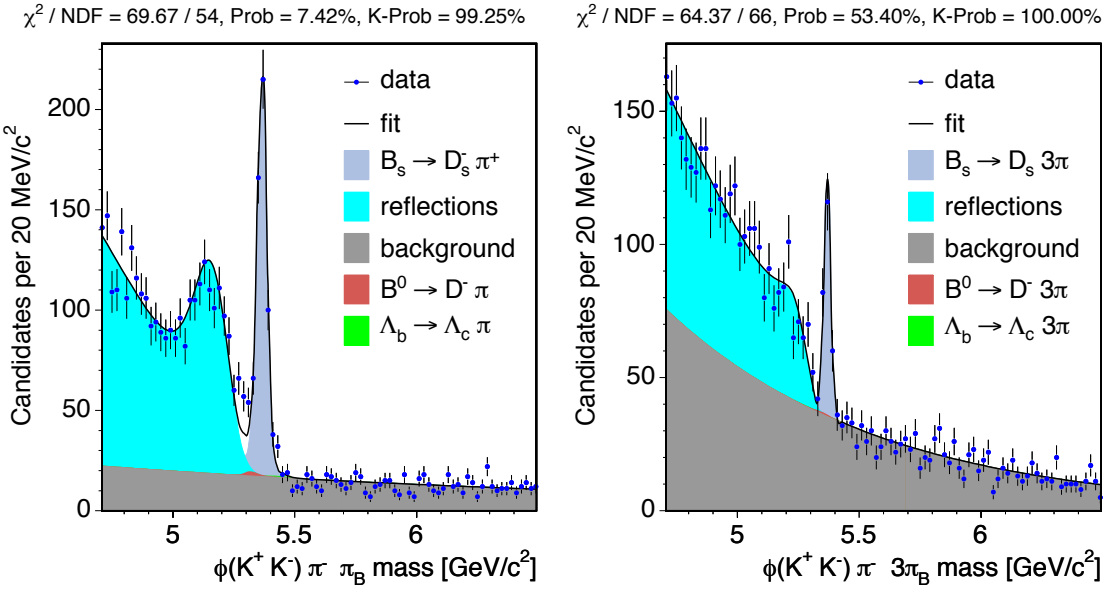

Figure 4.8: Wide range mass fits for $B_s \to D_s^-[\phi\pi^-]\pi^+$ (left) and $B_s \to D_s^-[\phi\pi^-]\pi^+(\pi^-\pi^+)$ (right) candidates.

a muon, and D stands for either of D^0, D^+, D^{*-}, and D_s^-, which are fully reconstructed.

None of the final states D^0l, D^+l, $D^{*+}l$ or D_sl is formed exclusively from a single, specific B decay mode. The reconstruction of the B meson is *partial*, with the neutrino and possibly other decay products being missed. Furthermore, the D^0l, D^+l, $D^{*+}l$ final states originate from a mixture of B^+ and B^0 decays through excited charm states. These inclusive modes are represented as follows,

- $B^{+,0} \to \bar{D}^0 l^+ X$, $\bar{D}^0 \to K^+\pi^-$,
- $B^{+,0} \to D^- l^+ X$, $D^- \to K^+\pi^-\pi^-$,
- $B^{+,0} \to D^{*-} l^+ X$, $D^{*-} \to \bar{D}^0\pi^-$, $\bar{D}^0 \to K^+\pi^-$,
- $B_s \to D_s^- l^+ X$, $D_s^- \to \phi\pi^-$,
- $B_s \to D_s^- l^+ X$, $D_s^- \to K^{*0}K^-$, $K^{*0} \to K^+\pi^-$,
- $B_s \to D_s^- l^+ X$, $D_s^- \to \pi^+\pi^-\pi^-$.

The $B \to Dl$ transition may not be direct, as the indicated final state may be achieved through a chain of intermediate states. X stands for the neutrino from the B semileptonic decay, and other unreconstructed decay products from intermediate channels.

This dissertation deals with the study of B properties, which are specific to the meson species: B^+, B^0, and B_s. In the inclusive samples, accordingly, we ought also to provide independent description for the three species. In particular, the relative fractions of B^+ and B^0 which contribute to each of the D^0l, D^+l, $D^{*+}l$ samples must be determined. The determination of these fractions, and corresponding uncertainties, is done based on the values of the so-called sample composition parameters, and the trigger and reconstruction efficiencies. This issue is addressed further below.

In the semileptonic decays, the mass of the complete B system cannot be determined due to the reconstruction being partial. Instead, the reconstructed mass of the involved D mesons is employed to describe the samples. There are several categories of background events which may mimic our semileptonic signals by providing both lepton and D candidates with the correct charge correlation. Certain physics processes involving B hadron decays other than the considered signal channels may contribute to the Dl signature. These are denoted by *physics* type background, and its contribution is evaluated from Monte Carlo simulation. Additionally, our Dl candidates may have contaminations resulting from incorrect reconstruction of either the D meson or the B-daughter lepton. Combinatorial background formed of events of the former class presents itself as a linear contribution in the D mass distribution. Events of the latter class are characterized using a sample obtained by selecting fake leptons and are thus denoted by *fakes* background.

Physics background

This class of background is realized by B hadron decays other than the semileptonic B signals which also feed into our Dl decay signatures. More specifically, this may correspond for instance to $B \to DDX$ decays where one of the charm mesons decays semileptonically. B decays to tau leptons with these decaying semileptonically are also part of this background class except in the case of the D_sl samples where $B_s \to \tau D_s X, \tau \to l\nu\nu$ decays are chosen and treated as a part of the signal. The relative overall contribution from these background components typically amounts up to 16% of the D_sl modes and to about 6% of the remaining Dl modes; such fractions are shown in Table 4.13 for the considered background components.

The contributions are evaluated, for each of the 24 semileptonic decay sub-samples, from a corresponding simulated inclusive physics background sample. These inclusive samples are obtained by generating Monte Carlo samples for each of the contributing background modes and weighting them according to the relevant branching fractions [1] and reconstruction efficiencies. The fractions are summarized in Table 4.14.

Fakes background and m_{Dl} analysis

This class of background arises from Dl candidates formed of a real D meson together with a track which may not be a real lepton or which did not really originate from a B decay. The lepton is said to be a *fake* in the former case, and in the latter it may have originated from a $c\bar{c}$ event.

The characterization of background events of this type may be attempted in few ways. One would be to explore the sample of wrongly correlated candidates, *e.g.* D^+l^+, given that no specific charge correlation between the D and l candidates is expected for events of the type mentioned above. This has in fact been explored in an earlier stage of the analysis. The method which we employ is based on a sample of fake leptons and real D events, which is obtained by applying lepton *anti*-selection; *i.e.* a sample in which the lepton track candidates are required to have low likelihood (specifically a lepton likelihood cut $\leq$0.05 is applied). The corresponding reconstructed D mass and Dl proper decay time distributions are illustrated in Figure 5.6.

The fraction of fakes background events in our samples is determined from a fit to the invariant mass distribution of the Dl pair candidates, m_{Dl}. Firstly, the combinatorial background component is subtracted, using the m_{Dl} distribution for D mass-sideband candidates. This distribution is then fitted with the model

$$f_{\text{fakes}} L^{\text{fakes}}_{m_{Dl}} + (1 - f_{\text{fakes}}) \left[f_{\text{phys.}} L^{\text{phys.}}_{m_{Dl}} + (1 - f_{\text{phys}}) L^{\text{signal}}_{m_{Dl}} \right], \tag{4.3}$$

where the $L_{m_{Dl}}$ and f denote the m_{Dl} templates and fractions of the indicated components. For the signal and the physics background these are determined from Monte Carlo simulation. The m_{Dl} template for the fakes background $L^{\text{fakes}}_{m_{Dl}}$ is obtained from the fake lepton sample after D mass-sideband subtraction. These various m_{Dl} distributions are illustrated in Figure 4.9. The background events have on average a significantly lower m_{Dl} than the signal events. The fraction f_{fakes} of the fakes background component which we set out to determine is the only free parameter in the fit, while the other two fraction are either fixed or constrained to the Monte Carlo values.

The fit is performed in the m_{Dl} range of $(2.05, 5.35)$ GeV/c^2 for the $D_s l$ samples, and of $(2.05, 5.50)$ GeV/c^2 for the other semileptonic samples. The input fractions and templates mentioned above are thus determined for these looser m_{Dl} selection criteria. The fit result for the f_{fakes} parameter is finally propagated into the nominal selection range $(2.9, 5.3)$ GeV/c^2 specified in Table 4.5. The final fakes background fractions are summarized in Table 4.15 for all Dl decay sub-samples.

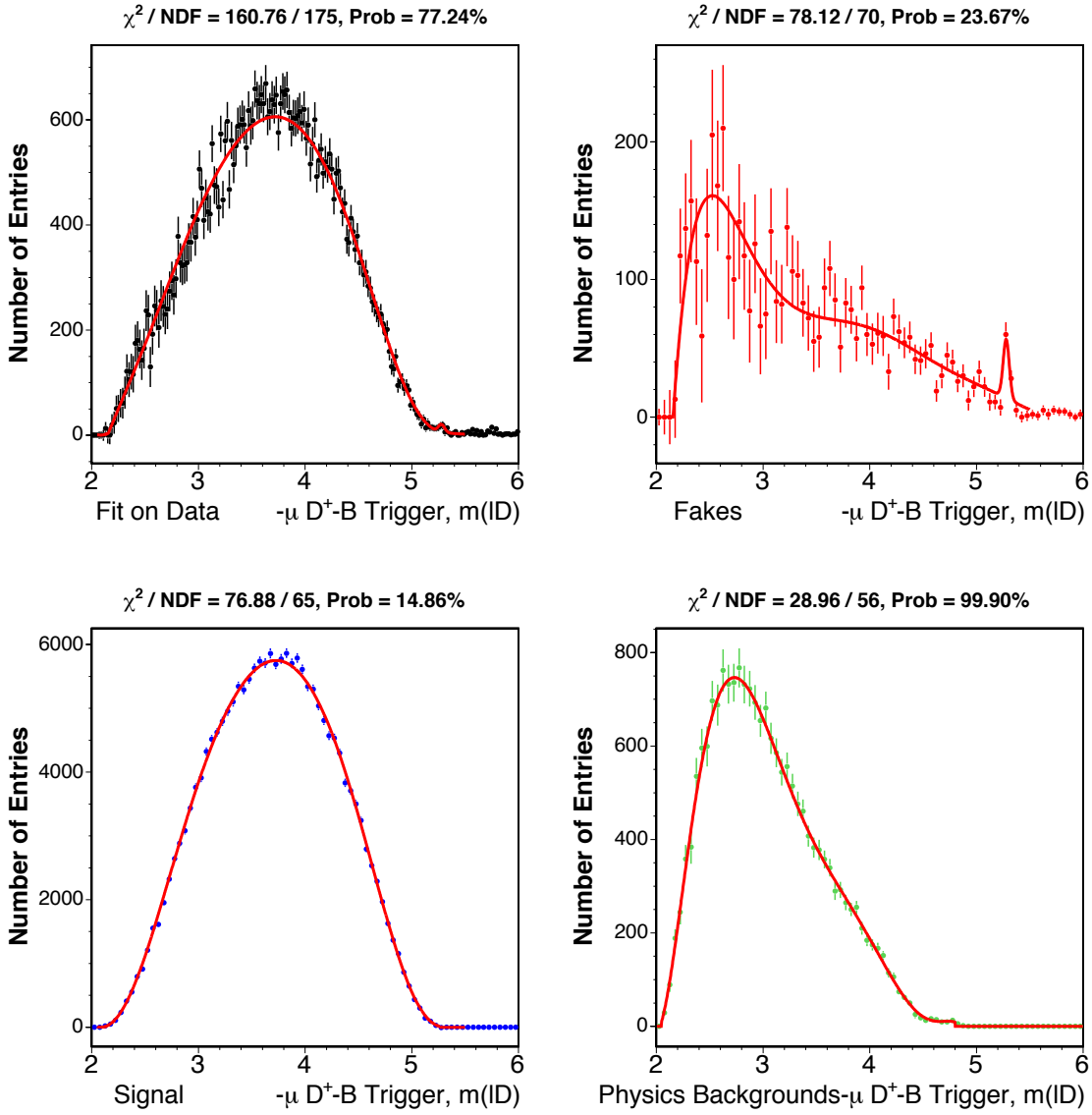

Figure 4.9: Fit to m_{Dl} [GeV/c^2] distribution on data (top left), together with templates for fake background (top right, from fake lepton sample), and signal and physics background (bottom left and bottom right, respectively, from Monte Carlo simulation). This is illustrated for the μD^+ B trigger sub-sample.

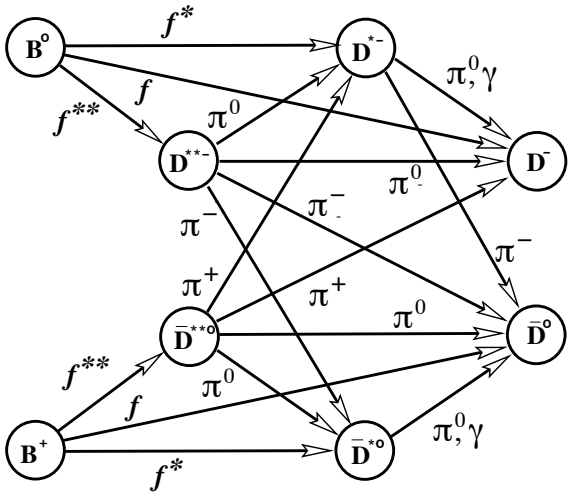

Figure 4.10: State diagram of $B^{+,0} \to DlX$ transitions.

Description of B^+ and B^0 content of $D^{(*)}l$ samples

The samples D^0l, D^+l, $D^{*+}l$ are formed of contributions from 24 decay chains of B^+ and B^0 mesons. These are illustrated schematically in Figure 4.10. The fraction of events with a signature k arising, say, from B^0 decays is obtained by performing a sum, over all B^0 decay chains h that contribute to that decay signature (k), of the product of the involved branching ratios with the selection efficiency; conceptually,

$$S_k^0 = \sum_{B^0 \to h \in k} \mathcal{B}(B \to lD^{(**)} \ldots) \times \mathcal{B}(D^{(**)} \to D^{(*)} \ldots) \times \ldots \times \mathcal{B}(D^+ \to K\pi\pi) \times \epsilon(B^0 \to h).$$

A similar expression S_k^+ may be obtained for B^+ decays. These relations as written depend upon absolute branching ratios and efficiencies, but by removing an overall normalization only relative fractions matter. Indeed, the contributing fraction from B^0 decays to a sample k is given by

$$f_k^0 = \frac{S_k^0}{S_k^0 + S_k^+}\,, \tag{4.4}$$

where efficiencies are expressed relative to that of the direct decay chain (*i.e.* $B \to Dl\nu$), and, for the most part, only ratios of branching ratios are needed.

The signal composition of the sample may for our purposes be characterized as follows. We denote by f, f^*, and f^{**} the relative fractions for B decaying into a D (*i.e.* D^0 or D^+), D^* (*i.e.* D^{*-} or D^{*0}), and D^{**} (*i.e.* an excited D state other than D^*), with $f + f^* + f^{**} = 1$. The rate that D^{**} states decay into D^* states relative to the rate that D^{**} states decay directly into D mesons is denoted by P_V. The efficiency for reconstructing the decay $D^{*-} \to \bar{D}^0\pi^-$ is represented by ϵ^*. The relative fractions of the individual decay chains are then given

in Table 4.17, in terms of the set of independent sample composition parameters shown in Table 4.16 – f^{**}, $R_f(\equiv f^*/f)$, P_V, ϵ^* – and the relevant branching fractions [1].

A needed correction for the sample composition, as referred to above, is the general effect of trigger and reconstruction efficiencies. The different decay chains are characterized by potentially different kinematic behavior, which results in different efficiencies for being selected at trigger or reconstruction levels, thus altering the decay chains relative contribution to a given decay signature. Since only relative efficiencies are involved as noted above, many uncertainties cancel in the calculation. These efficiencies are determined from 21 signal Monte Carlo samples, and given in Table 4.18, for each lD sample, relative to the corresponding direct decay mode.

$B^+ \to J/\psi K^+$,	$J/\psi \to \mu^+\mu^-$
$B^0 \to J/\psi K^{*0}$,	$J/\psi \to \mu^+\mu^-$, $K^{*0} \to K^+\pi^-$
$B^+ \to \bar{D}^0\pi^+$,	$\bar{D}^0 \to K^+\pi^-$
$B^+ \to \bar{D}^0\pi^+\pi^-\pi^+$,	$\bar{D}^0 \to K^+\pi^-$
$B^0 \to D^-\pi^+$,	$D^- \to K^+\pi^-\pi^-$
$B^0 \to D^-\pi^+\pi^-\pi^+$,	$D^- \to K^+\pi^-\pi^-$
$B^0 \to D^{*-}\pi^+$,	$D^{*-} \to \bar{D}^0\pi^-$, $\bar{D}^0 \to K^+\pi^-$
$B^0 \to D^{*-}\pi^+$,	$D^{*-} \to \bar{D}^0\pi^-$, $\bar{D}^0 \to K^+\pi^-\pi^+\pi^-$
$B^0 \to D^{*-}\pi^+\pi^-\pi^+$,	$D^{*-} \to \bar{D}^0\pi^-$, $\bar{D}^0 \to K^+\pi^-$
$B^0 \to D^{*-}\pi^+\pi^-\pi^+$,	$D^{*-} \to \bar{D}^0\pi^-$, $\bar{D}^0 \to K^+\pi^-\pi^+\pi^-$
$B_s \to D_s^-\pi^+$,	$D_s^- \to \phi\pi^-$, $\phi \to K^+K^-$
$B_s \to D_s^-\pi^+$,	$D_s^- \to K^{*0}K^-$, $K^{*0} \to K^+\pi^-$
$B_s \to D_s^-\pi^+$,	$D_s^- \to \pi^-\pi^+\pi^-$
$B_s \to D_s^-\pi^+\pi^-\pi^+$,	$D_s^- \to \phi\pi^-$, $\phi \to K^+K^-$
$B_s \to D_s^-\pi^+\pi^-\pi^+$,	$D_s^- \to K^{*0}K^-$, $K^{*0} \to K^+\pi^-$
$B^{+,0} \to \bar{D}^0 l^+ X$,	$\bar{D}^0 \to K^+\pi^-$
$B^{+,0} \to D^- l^+ X$,	$D^- \to K^+\pi^-\pi^-$
$B^{+,0} \to D^{*-} l^+ X$,	$D^{*-} \to \bar{D}^0\pi^-$, $\bar{D}^0 \to K^+\pi^-$
$B_s \to D_s^- l^+ X$,	$D_s^- \to \phi\pi^-$, $\phi \to K^+K^-$
$B_s \to D_s^- l^+ X$,	$D_s^- \to K^{*0}K^-$, $K^{*0} \to K^+\pi^-$
$B_s \to D_s^- l^+ X$,	$D_s^- \to \pi^-\pi^+\pi^-$

Table 4.1: The full list of decay channels analyzed.

decays	$B^+ \to J/\psi K^+$	$B^0 \to J/\psi K^{*0}$
B vertex probability >	10^{-3}	10^{-4}
$p_T(B)$ [GeV/c] >	5.5	6.0
$p_T(K^{*0,+})$ [GeV/c] >	1.6	2.6
σ_{ct} [μm] <	150	150

Table 4.2: Summary of reconstruction requirements for $J/\psi K$ samples.

	B^+ modes		B^0 modes			
	$\bar{D}^0\pi^+$	$\bar{D}^0\pi^+\pi^-\pi^+$	$D^-\pi^+$	$D^-\pi^+\pi^-\pi^+$	$D^{*-}\pi^+$	$D^{*-}\pi^+\pi^-\pi^+$
$\chi^2_{r\phi}(B)$ <	15	8	15	11	17	20
$\chi^2_{r\phi}(D)$ <	15	4	15	15	16	16
$\chi^2_{r\phi}(\pi\pi\pi)$ <	—	6	—	—	—	—
$\sigma_{L_{xy}}(B)$ [μm] <	—	—	—	—	200	200
$\frac{L_{xy}}{\sigma}(B)$ >	8	15	11	14	4.5	8
$\frac{L_{xy}}{\sigma}(D)$ >	—	10	—	14	3	6
$L_{xy}(B \to D)$ [μm] >	-150	0	-300	0	—	—
$\lvert d_0(B)\rvert$ [μm] <	80	55	110	70	180	180
$p_T(B)$ [GeV/c^2] >	5.5	8.5	5.5	7.0	4.0	9.0
$p_T(\pi_B)$ [GeV/c^2] >	1.0	—	1.2	—	1.5	0.4
$p_T(\pi_{soft})$ [GeV/c^2] >	—	—	—	—	0.4	0.4
$m_{3\pi}$, GeV/c^2 <	—	1.75	—	—	—	2.3
$\lvert\Delta M_{D^*} - 145.4\rvert$ [MeV/c^2] <	—	—	—	—	2.5	2.5
$\Delta R(D, \pi_B)$ <	2.0	—	1.5	—	—	—

Table 4.3: Summary of reconstruction requirements for $D^{(*)}\pi(\pi\pi)$ samples; D^* decays with both $D^0 \to K\pi$ and $D^0 \to K\pi\pi\pi$ are included.

$B_s \to \ldots$		$D_s^- \pi^+$			$D_s^- \pi^+ \pi^- \pi^+$	
$D_s \to \ldots$		$\phi\pi^-$	$K^{*0}K^-$	3π	$\phi\pi^-$	$K^{*0}K^-$
$\chi^2_{r\phi}(B)$	$<$	15	8	6	15	8
$\chi^2_{r\phi}(D)$	$<$	14	15	15	15	10
$\sigma_{L_{xy}}(B)$ [μm]	$<$	400	400	400	400	400
$\frac{L_{xy}}{\sigma}(B)$	$>$	7	9	13	11	18
$\frac{L_{xy}}{\sigma}(D)$	$>$	2	2	2	11	15
$L_{xy}(B \leftarrow D)$ [μm]	$>$	-200	-200	-100	-50	100
$\lvert d_0(B)\rvert$ [μm]	$<$	60	60	60	70	50
$p_T(B)$ [GeV/c^2]	$>$	5.5	5.5	6.0	6.0	5.0
$p_T(\pi_B)$ [GeV/c^2]	$>$	1.2	1.3	1.5	—	—
$p_T(K^\pm, \pi^\pm)$ [GeV/c^2]	$>$	0.35	0.40	0.40	0.45	0.35
m_{KK}, [GeV/c^2]		[1.013,1.28]	—	—	[1.010,1.031]	—
$\lvert m_{K\pi} - m_{K^*}\rvert$ [MeV/c^2]	$<$	—	55	—	—	50
$\lvert m_{KK\pi} - m_{D_s}\rvert$ [MeV/c^2]	$<$	—	25	—	—	—
$\lvert m_{K\pi\pi} - m_{D^-}\rvert$ [MeV/c^2]	$>$	—	24	—	—	24
$\lvert m_{K\pi\pi} - m_{K\pi}\rvert$ [MeV/c^2]	$>$	—	—	160	—	—
$\Delta R(D, \pi_B)$	$<$	—	1.5	1.5	—	—

Table 4.4: Summary of reconstruction requirements for $D_s\pi(\pi\pi)$ samples.

.

	lD^0	lD^+	$lD_s[\phi\pi^-]$	$lD_s[K^{*0}K^-]$	$lD_s[\pi^+\pi^-\pi^-]$
B vertex probability $>$	10^{-6}	10^{-5}	10^{-7}	10^{-5}	10^{-5}
$\chi^2_{xy}(D)$ $<$	20	20	20	20	20
$L_{xy}/\sigma_{L_{xy}}(D \to PV)$ $>$	6	11	5	8	11
$L_{xy}/\sigma_{L_{xy}}(D \to PV)$ $>$	2	2	—	2	2
$\lvert cos\,\psi\rvert$ $>$	—	—	0.3	0.3	—
$p_T(K^\pm, \pi^\pm)$ [GeV/c] $>$	0.5	0.7	0.7	0.7	0.7
m_{lD} [GeV/c^2]	2.9 - 5.3	2.9 - 5.3	2.9 - 5.3	2.9 - 5.3	2.9 - 5.3

Table 4.5: Summary of reconstruction requirements for Dl samples; the requirements for the D^*l sample are identical to those of the D^0l sample.

sample	N_S
$B^+ \to J/\psi K^+$	4,950
$B^+ \to \bar{D}^0\pi^+$	9,600
$B^+ \to \bar{D}^0\pi^\pm$	1,560
$B^0 \to J/\psi K^{*0}$	1,790
$B^0 \to D^-\pi^+$	8,420
$B^0 \to D^-\pi^+\pi^-\pi^+$	4,610
$B^0 \to D^{*-}\pi^+$ ($\bar{D}^0 \to K^+\pi^-$)	1,380
$B^0 \to D^{*-}\pi^+$ ($\bar{D}^0 \to K^+\pi^-\pi^+\pi^-$)	1,010
$B^0 \to D^{*-}\pi^+\pi^-\pi^+$ ($\bar{D}^0 \to K^+\pi^-$)	1,090
$B^0 \to D^{*-}\pi^+\pi^-\pi^+$ ($\bar{D}^0 \to K^+\pi^-\pi^+\pi^-$)	820
$B_s \to D_s^-\pi^+$, $D_s \to \phi\pi$	550
$B_s \to D_s^-\pi^+$, $D_s \to K^*K$	240
$B_s \to D_s^-\pi^+$, $D_s \to 3\pi$	110
$B_s \to D_s^-\pi^+\pi^-\pi^+$, $D_s \to \phi\pi$	160
$B_s \to D_s^-\pi^+\pi^-\pi^+$, $D_s \to K^*K$	60

Table 4.6: Summary of the estimated signal event yields for the fully reconstructed samples.

sub-sample	trigger type	N_S	sub-sample	trigger type	N_S
μD^0	B	103,300	$\mu D_s[\phi\pi^-]$	B	5,230
μD^0	D	18,100	$\mu D_s[\phi\pi^-]$	D	1,150
μD^+	B	11,300	$\mu D_s[K^{*0}K^-]$	B	1,750
μD^+	D	3,200	$\mu D_s[K^{*0}K^-]$	D	650
μD^*	B	47,800	$\mu D_s[\pi^+\pi^-\pi^-]$	B	1,530
μD^*	D	13,400	$\mu D_s[\pi^+\pi^-\pi^-]$	D	750
eD^0	B	53,800	$eD_s[\phi\pi^-]$	B	2,910
eD^0	D	10,200	$eD_s[\phi\pi^-]$	D	720
eD^+	B	6,400	$eD_s[K^{*0}K^-]$	B	970
eD^+	D	1,900	$eD_s[K^{*0}K^-]$	D	360
eD^*	B	26,400	$eD_s[\pi^+\pi^-\pi^-]$	B	850
eD^*	D	7,600	$eD_s[\pi^+\pi^-\pi^-]$	D	340

Table 4.7: Summary of the signal event yields per Dl sub-sample.

	$B^+ \to J/\psi K^+$	$B^0 \to J/\psi K^{*0}$
$B^+ \to J/\psi \pi^+$	2.50 ± 0.06 %	-
$K^{*0}(K \leftrightarrow \pi)$ swap	-	16.9±0.4 %

Table 4.8: Contributions from non-combinatorial components in the $J/\psi K$ samples relative to the nominal signals.

partially-reconstructed fractions			
$B^+ \to \bar{D}^0\pi^+$	–	$B_s \to D_s^-[\phi\pi^-]\pi^+$	0.59 %
$B^+ \to \bar{D}^0\pi^+\pi^-\pi^+$	–	$B_s \to D_s^-[K^{*0}K^-]\pi^+$	2.67 %
$B^0 \to D^-\pi^+$	–	$B_s \to D_s^-[\pi^-\pi^+\pi^-]\pi^+$	0.66 %
$B^0 \to D^-\pi^+\pi^-\pi^+$	–	$B_s \to D_s^-[\phi\pi^-]\pi^+(\pi^-\pi^+)$	0.99 %
$B^0 \to D^{*-}\pi^+\pi^-\pi^+$	–	$B_s \to D_s^-[K^{*0}K^-]\pi^+(\pi^-\pi^+)$	0.41 %

Table 4.9: Contributions from partially reconstructed backgrounds to the $B \to D\pi(\pi\pi)$ samples; the relative fractions are calculated in the narrow mass range, from Monte Carlo simulation.

cabibbo-suppressed fractions			
$B^+ \to \bar{D}^0\pi^+$	6.16 %	$B_s \to D_s^-[\phi\pi^-]\pi^+$	6.09 %
$B^+ \to \bar{D}^0\pi^+\pi^-\pi^+$	7.87 %	$B_s \to D_s^-[K^{*0}K^-]\pi^+$	5.66 %
$B^0 \to D^-\pi^+$	5.80 %	$B_s \to D_s^-[\pi^-\pi^+\pi^-]\pi^+$	5.95 %
$B^0 \to D^-\pi^+\pi^-\pi^+$	6.68 %	$B_s \to D_s^-[\phi\pi^-]\pi^+(\pi^-\pi^+)$	5.00 %
$B^0 \to D^{*-}\pi^+$	6.34 %	$B_s \to D_s^-[K^{*0}K^-]\pi^+(\pi^-\pi^+)$	5.00 %
$B^0 \to D^{*-}\pi^+\pi^-\pi^+$	–		

Table 4.10: Contributions from Cabibbo-suppressed components to the $B \to D\pi(\pi\pi)$ samples; the relative fractions are calculated in the narrow mass range, from Monte Carlo simulation.

$B_s \to \ldots$	$D_s^-[\phi\pi^-]\pi^+$	$D_s^-[K^{*0}K^-]\pi^+$	$D_s^-[\pi^-\pi^+\pi^-]\pi^+$
$B_s \to D_s^-[\phi\pi^-]\pi^+$	1	$0.249 \pm 0.075\%$	–
$B_s \to D_s^-[K^{*0}K^-]\pi^+$	$0.233 \pm 0.064\%$	1	–
$B_s \to D_s^-[\pi^-\pi^+\pi^-]\pi^+$	–	$0.0073 \pm 0.0063\%$	1
$B^0 \to D^-[K^+\pi^-\pi^-]\pi^+$	$1.26 \pm 0.40\%$	$1.88 \pm 0.29\%$	$0.0587 \pm 0.0092\%$
$\Lambda_b \to \Lambda_c^+[pK^-\pi^+]\pi^-$	$0.598 \pm 0.21\%$	$11.6 \pm 1.9\%$	–
$\Lambda_b \to \Lambda_c^+[p\pi^-\pi^+]\pi^-$	$0.0180 \pm 0.0039\%$	$0.236 \pm 0.039\%$	$5.16 \pm 0.85\%$

Table 4.11: Contributions from fully reconstructed backgrounds to the $B_s \to D_s^-\pi^+$ samples; the fractions are calculated in the narrow mass range, from Monte Carlo simulation.

$B_s \to \ldots$	$D_s^-[\phi\pi^-]\pi^+\pi^-\pi^+$	$D_s^-[K^{*0}K^-]\pi^+\pi^-\pi^+$
$B_s \to D_s^-[\phi\pi^-]\pi^+(\pi^-\pi^+)$	1	0.55 ± 0.21 %
$B_s \to D_s^-[K^{*0}K^-]\pi^+(\pi^-\pi^+)$	0.371 ± 0.13 %	1
$B^0 \to D^-[K^+\pi^-\pi^-]\pi^+(\pi^-\pi^+)$	1.91 ± 0.87 %	6.3 ± 2.8 %
$\Lambda_b \to \Lambda_c^+[pK^-\pi^+]\pi^-(\pi^+\pi^-)$	1.16 ± 0.19 %	14.2 ± 2.4 %
$\Lambda_b \to \Lambda_c^+[p\pi^-\pi^+]\pi^-(\pi^+\pi^-)$	0.076 ± 0.013 %	0.43 ± 0.071 %

Table 4.12: Contributions from fully reconstructed backgrounds to the $B_s \to D_s^-\pi^+\pi^-\pi^+$ samples; the fractions are calculated in the narrow mass range, from Monte Carlo simulation.

decay		$\phi\pi^-$ [%]	$K^{*0}K^-$ [%]	$\pi^+\pi^-\pi^-$ [%]
$B_s \to D_s^{(*)} D^{(*)} X$,	$D^{(*)} \to \mu^+ X$	—	—	—
$B_s \to D_s^{(*+)} D_s^{(*-)} X$,	$D_s^{(*)} \to \mu^+ X$	3.0 ± 0.9	3.0 ± 0.9	2.9 ± 0.9
$B^+ \to D_s^{(*)} D^{(*)} X$,	$D^{(*)} \to \mu^+ X$	6.2 ± 2.5	6.2 ± 2.5	6.0 ± 2.4
$B^0 \to D_s^{(*)} D^{(*)} X$,	$D^{(*)} \to \mu^+ X$	6.3 ± 2.5	6.3 ± 2.5	6.0 ± 2.4
total		15.5 ± 3.6	15.5 ± 3.6	14.9 ± 3.5
$B_s \to D_s^{(*)} D^{(*)} X$,	$D^{(*)} \to e^+ X$	—	—	—
$B_s \to D_s^{(*+)} D_s^{(*-)} X$,	$D_s^{(*)} \to e^+ X$	2.1 ± 0.6	2.3 ± 0.7	1.7 ± 0.5
$B^+ \to D_s^{(*)} D^{(*)} X$,	$D^{(*)} \to e^+ X$	5.4 ± 2.2	5.1 ± 2.0	5.2 ± 2.1
$B^0 \to D_s^{(*)} D^{(*)} X$,	$D^{(*)} \to e^+ X$	5.3 ± 2.1	5.0 ± 2.0	5.1 ± 2.0
total		12.8 ± 3.1	12.4 ± 3.0	12.0 ± 2.9

Table 4.13: Expected fraction of each physics background component, relative to the sum of signal and physics background, for each selected D_s decay mode, and for muons and electrons separately (averaged over B and D trigger types).

physics background					
sub-sample	trigger type	fraction [%]	sub-sample	trigger type	fraction [%]
μD^0	B	14.8 ± 5.0	$\mu D_s[\phi\pi^-]$	B	14.8 ± 5.0
μD^0	D	18.1 ± 6.2	$\mu D_s[\phi\pi^-]$	D	18.1 ± 6.2
μD^+	B	14.7 ± 5.0	$\mu D_s[K^{*0}K^-]$	B	14.7 ± 5.0
μD^+	D	17.8 ± 6.2	$\mu D_s[K^{*0}K^-]$	D	17.8 ± 6.2
μD^*	B	14.2 ± 4.9	$\mu D_s[\pi^+\pi^-\pi^-]$	B	14.2 ± 4.9
μD^*	D	16.3 ± 5.7	$\mu D_s[\pi^+\pi^-\pi^-]$	D	16.3 ± 5.7
eD^0	B	10.2 ± 3.6	$eD_s[\phi\pi^-]$	B	10.2 ± 3.6
eD^0	D	17.7 ± 6.1	$eD_s[\phi\pi^-]$	D	17.7 ± 6.1
eD^+	B	8.7 ± 3.0	$eD_s[K^{*0}K^-]$	B	8.7 ± 3.0
eD^+	D	10.4 ± 3.6	$eD_s[K^{*0}K^-]$	D	10.4 ± 3.6
eD^*	B	11.9 ± 4.1	$eD_s[\pi^+\pi^-\pi^-]$	B	11.9 ± 4.1
eD^*	D	9.4 ± 3.2	$eD_s[\pi^+\pi^-\pi^-]$	D	9.4 ± 3.2

Table 4.14: Fractions of physics background, for all 24 semileptonic decay sub-samples, with respect to the sum of signal and physics background.

fakes background					
sub-sample	trigger type	fraction [%]	sub-sample	trigger type	fraction [%]
μD^0	B	2.4 ± 0.5	$\mu D_s[\phi\pi^-]$	B	2.7 ± 0.6
μD^0	D	6.8 ± 1.4	$\mu D_s[\phi\pi^-]$	D	7.7 ± 1.8
μD^+	B	2.5 ± 0.5	$\mu D_s[K^{*0}K^-]$	B	3.7 ± 0.8
μD^+	D	6.3 ± 1.3	$\mu D_s[K^{*0}K^-]$	D	8.7 ± 1.9
μD^*	B	2.0 ± 0.4	$\mu D_s[\pi^+\pi^-\pi^-]$	B	4.4 ± 0.9
μD^*	D	5.3 ± 1.1	$\mu D_s[\pi^+\pi^-\pi^-]$	D	7.7 ± 1.7
eD^0	B	1.9 ± 0.5	$eD_s[\phi\pi^-]$	B	4.0 ± 0.9
eD^0	D	7.0 ± 1.4	$eD_s[\phi\pi^-]$	D	8.8 ± 1.9
eD^+	B	2.1 ± 0.4	$eD_s[K^{*0}K^-]$	B	2.1 ± 0.5
eD^+	D	8.9 ± 1.8	$eD_s[K^{*0}K^-]$	D	8.9 ± 2.0
eD^*	B	2.0 ± 0.4	$eD_s[\pi^+\pi^-\pi^-]$	B	3.5 ± 0.8
eD^*	D	5.1 ± 1.0	$eD_s[\pi^+\pi^-\pi^-]$	D	7.3 ± 1.7

Table 4.15: Fractions of fakes background, for all 24 semileptonic decay sub-samples, with respect to the sum of signal with fakes and physics backgrounds.

R_f	2.14 ± 0.14
f^{**}	0.31 ± 0.05
P_V	0.627 ± 0.26

Table 4.16: Semileptonic $B^{+,0}$ signal composition parameters.

	decay signatures		
	$D^{*-}l$	$D^{-}l$	$D^{0}l$
B^+ decay chains			
$\to \overline{D}^{**0} l^+\nu$			
$\overline{D}^{**0} \to D^{*-}\pi^+_{**}$			
$D^{*-} \to \overline{D}^0\pi^-_*$	$f^{**}P_V\frac{2}{3}\mathcal{B}^*(\overline{D}^0\pi^-_*)\epsilon^*$	—	$f^{**}P_V\frac{2}{3}\mathcal{B}^*(\overline{D}^0\pi^-_*)(1-\epsilon^*)$
$D^{*-} \to D^-\pi^0_*$	—	$f^{**}P_V\frac{2}{3}\mathcal{B}^*(D^-\pi^0_*)$	—
$D^{*-} \to \overline{D}^0\gamma$	—	$f^{**}P_V\frac{2}{3}\mathcal{B}^*(D^-\gamma)$	—
$\overline{D}^{**0} \to \overline{D}^{*0}\pi^0_{**}$			
$\overline{D}^{*0} \to \overline{D}^0\pi^0_*$	—	—	$f^{**}P_V\frac{1}{3}\mathcal{B}^*(\overline{D}^0\pi^0_*)$
$\overline{D}^{*0} \to \overline{D}^0\gamma$	—	—	$f^{**}P_V\frac{1}{3}\mathcal{B}^*(\overline{D}^0\gamma)$
$\overline{D}^{**0} \to D^-\pi^+_{**}$	—	$f^{**}(1-P_V)\frac{2}{3}$	—
$\overline{D}^{**0} \to \overline{D}^0\pi^0_{**}$	—	—	$f^{**}(1-P_V)\frac{1}{3}$
$\to \overline{D}^{*0} l^+\nu$			
$\overline{D}^{*0} \to \overline{D}^0\pi^0_*$	—	—	$f^*\mathcal{B}^*(\overline{D}^0\pi^0_*)$
$\overline{D}^{*0} \to \overline{D}^0\gamma$	—	—	$f^*\mathcal{B}^*(\overline{D}^0\gamma)$
$\to \overline{D}^0 l^+\nu$	—	—	f
B^0 decay chains			
$\to D^{**-} l^+\nu$			
$D^{**-} \to \overline{D}^{*0}\pi^-_{**}$			
$\overline{D}^{*0} \to \overline{D}^0\pi^0_*$	—	—	$f^{**}P_V\frac{2}{3}\mathcal{B}^*(D^-\pi^0_*)$
$\overline{D}^{*0} \to \overline{D}^0\gamma$	—	—	$f^{**}P_V\frac{2}{3}\mathcal{B}^*(\overline{D}^0\gamma)$
$D^{**-} \to D^{*-}\pi^0_{**}$			
$D^{*-} \to \overline{D}^0\pi^-_*$	$f^{**}P_V\frac{1}{3}\mathcal{B}^*(\overline{D}^0\pi^-_*)\epsilon^*$	—	$f^{**}P_V\frac{1}{3}\mathcal{B}^*(\overline{D}^0\pi^-_*)(1-\epsilon^*)$
$D^{*-} \to D^-\pi^0_*$	—	$f^{**}P_V\frac{1}{3}\mathcal{B}^*(D^-\pi^0_*)$	—
$D^{*-} \to D^-\gamma$	—	$f^{**}P_V\frac{1}{3}\mathcal{B}^*(D^-\gamma)$	—
$D^{**-} \to \overline{D}^0\pi^-_{**}$	—	—	$f^{**}(1-P_V)\frac{2}{3}$
$D^{**-} \to D^-\pi^0_{**}$	—	$f^{**}(1-P_V)\frac{1}{3}$	—
$\to D^{*-} l^+\nu$			
$D^{*-} \to \overline{D}^0\pi^-_*$	$f^*\mathcal{B}^*(\overline{D}^0\pi^-_*)\epsilon^*$	—	$f^*\mathcal{B}^*(\overline{D}^0\pi^-_*)(1-\epsilon^*)$
$D^{*-} \to D^-\pi^0_*$	—	$f^*\mathcal{B}^*(D^-\pi^0_*)$	—
$D^{*-} \to D^-\gamma$	—	$f^*\mathcal{B}^*(D^-\gamma)$	—
$\to D^- l^+\nu$	—	f	—

Table 4.17: The various B^+ and B^0 decay chains and their contributions to the composition of the three general categories of decay signatures ($D^{*-}l$, $D^{-}l$, and $\bar{D}^0 l$); the branching ratio of $D^* \to X$ is denoted by "$\mathcal{B}^*(X)$".

	decay chain					relative efficiencies	
						trigger	reconstruction
$D^0 l$	$B^0 \to$		$D^{*-} \to$	$\pi_*^- \overline{D}^0 \to$	$K\pi$	1.22 ± 0.02	0.90 ± 0.01
	$B^0 \to$	$D^{**-} \to$	$\pi_{**}^0 D^{*-} \to$	$\pi_*^- \overline{D}^0 \to$	$K\pi$	0.85 ± 0.01	0.92 ± 0.01
	$B^0 \to$	$D^{**-} \to$	π_{**}^-	$\overline{D}^0 \to$	$K\pi$	0.95 ± 0.01	0.91 ± 0.01
	$B^0 \to$	$D^{**-} \to$	$\pi_{**}^- D^{*0} \to$	$\gamma \overline{D}^0 \to$	$K\pi$	0.83 ± 0.01	0.92 ± 0.01
	$B^0 \to$	$D^{**-} \to$	$\pi_{**}^- D^{*0} \to$	$\pi_*^0 \overline{D}^0 \to$	$K\pi$	0.84 ± 0.01	0.91 ± 0.01
	$B^+ \to$			$\overline{D}^0 \to$	$K\pi$	1	1
	$B^+ \to$		$D^{*0} \to$	$\gamma \overline{D}^0 \to$	$K\pi$	1.32 ± 0.02	0.93 ± 0.01
	$B^+ \to$		$D^{*0} \to$	$\pi_*^0 \overline{D}^0 \to$	$K\pi$	1.32 ± 0.02	0.93 ± 0.01
	$B^+ \to$	$\overline{D}^{**0} \to$	π_{**}^0	$\overline{D}^0 \to$	$K\pi$	0.83 ± 0.01	0.94 ± 0.01
	$B^+ \to$	$\overline{D}^{**0} \to$	$\pi_{**}^0 \overline{D}^{*0} \to$	$\gamma \overline{D}^0 \to$	$K\pi$	0.94 ± 0.01	0.95 ± 0.01
	$B^+ \to$	$\overline{D}^{**0} \to$	$\pi_{**}^0 \overline{D}^{*0} \to$	$\pi_*^0 \overline{D}^0 \to$	$K\pi$	0.84 ± 0.01	0.93 ± 0.01
	$B^+ \to$	$\overline{D}^{**0} \to$	$\pi_{**}^+ D^{*-} \to$	$\pi_*^- \overline{D}^0 \to$	$K\pi$	0.83 ± 0.01	0.91 ± 0.01
$D^- l$	$B^0 \to$			$D^- \to$	$K\pi\pi$	1	1
	$B^0 \to$		$D^{*-} \to$	$\gamma D^- \to$	$K\pi\pi$	1.20 ± 0.02	0.96 ± 0.01
	$B^0 \to$		$D^{*-} \to$	$\pi_*^0 D^- \to$	$K\pi\pi$	1.19 ± 0.02	0.96 ± 0.01
	$B^0 \to$	$D^{**-} \to$	π_{**}^0	$D^- \to$	$K\pi\pi$	0.85 ± 0.01	0.95 ± 0.01
	$B^0 \to$	$D^{**-} \to$	$\pi_{**}^0 D^{*-} \to$	$\gamma D^- \to$	$K\pi\pi$	0.78 ± 0.01	0.97 ± 0.01
	$B^0 \to$	$D^{**-} \to$	$\pi_{**}^0 D^{*-} \to$	$\pi_*^0 D^- \to$	$K\pi\pi$	0.78 ± 0.01	0.95 ± 0.01
	$B^+ \to$	$\overline{D}^{**0} \to$	π_{**}^+	$D^- \to$	$K\pi\pi$	1.06 ± 0.02	0.77 ± 0.01
	$B^+ \to$	$\overline{D}^{**0} \to$	$\pi_{**}^+ D^{*-} \to$	$\gamma D^- \to$	$K\pi\pi$	0.91 ± 0.01	0.82 ± 0.01
	$B^+ \to$	$\overline{D}^{**0} \to$	$\pi_{**}^+ D^{*-} \to$	$\pi_*^0 D^- \to$	$K\pi\pi$	0.91 ± 0.01	0.81 ± 0.01
$D^{*-} l$	$B^0 \to$		$D^{*-} \to$	$\pi_*^- \overline{D}^0 \to$	$K\pi$	1	1
	$B^0 \to$	$D^{**-} \to$	$\pi_{**}^0 D^{*-} \to$	$\pi_*^- \overline{D}^0 \to$	$K\pi$	0.68 ± 0.01	1.05 ± 0.02
	$B^+ \to$	$\overline{D}^{**0} \to$	$\pi_{**}^+ D^{*-} \to$	$\pi_*^- \overline{D}^0 \to$	$K\pi$	0.66 ± 0.01	0.99 ± 0.02

Table 4.18: Relative trigger and reconstruction efficiencies of the 21 B^+ and B^0 signal decay chains.

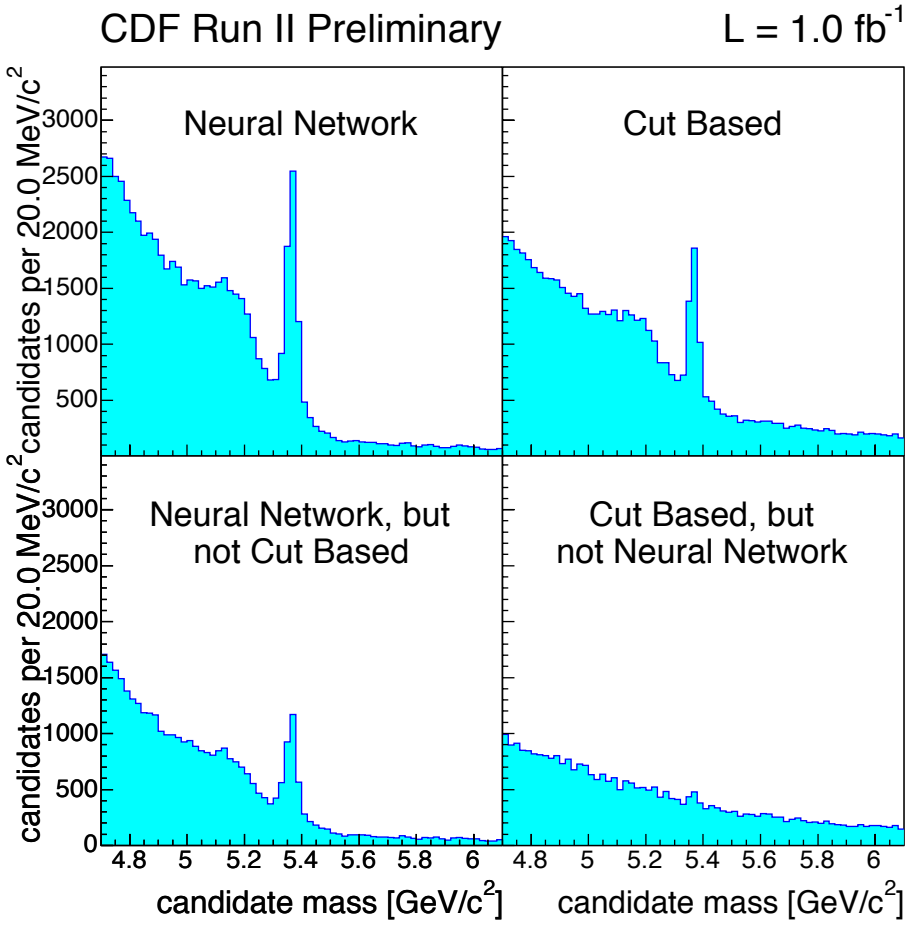

Figure 4.11: Illustration of the gain in signal yield extraction via the usage of an artificial neural network in event selection.

4.4 The full dataset

The development of all of the core aspects of the analysis took place while the bulk of the dataset was simultaneously being collected. In particular, the dataset corresponding to the first $355\,\mathrm{pb}^{-1}$, that was collected from February 2002 to August 2004, is employed for establishing the various tecnhiques and foundation of the analysis, and will yield also the first significant B_s oscillation signal. This fact is reflected on the forthcoming chapters where the results reported are those extracted therefrom. The extension to the full $1\,\mathrm{fb}^{-1}$ datset is subsequently performed, and leads noticeably in Chapter 10 to the final B_s analysis results.

The raw increase in statistics, which characterizes the larger dataset, is further enhanced

by additional optimization of the signal selection. Indeed, the better understanding of the data that has been acquired along with progress in the calibration of the detector systems facilitate the usage of more complex algorithms. One of these occurs at the level of particle identification. Specifically, measurements of specific ionization (dE/dx) and flight time (TOF) are combined (9.2) and utilized to assist in kaon selection. The addition of such an observable allows for relaxing kinematic selection requirements on the D_s decay products. The use of multivariate methods becomes at this point appropriate as well. For the case of the hadronic modes, an artificial neural network (ANN) is explored to more efficiently combine the selection criteria. The network is trained using Monte Carlo simulated signals, and backgrounds from mass sidebands in data. An improvement in signal extraction using this method is illustrated in Figure 4.11.

The extracted signal yields and mass distributions corresponding to the full $1\,\mathrm{fb}^{-1}$ dataset are shown in Table 4.19 and Figure 4.12, for the hadronic modes, and Table 4.20 and Figure 4.13, for the semileptonic modes, respectively.

decay sequence	S	S/B
$B_s \to D_s^- \pi^+$, $D_s^- \to \phi\pi^-$	1,900	11.3
$B_s \to D_s^- \pi^+$, $D_s^- \to K^{*0}K^-$	1,400	2.0
$B_s \to D_s^- \pi^+$, $D_s^- \to \pi^-\pi^+\pi^-$	700	2.1
$B_s \to D_s^- \pi^+\pi^-\pi^+$, $D_s^- \to \phi\pi^-$	700	2.7
$B_s \to D_s^- \pi^+\pi^-\pi^+$, $D_s^- \to K^{*0}K^-$	600	1.1
$B_s \to D_s^- \pi^+\pi^-\pi^+$, $D_s^- \to \pi^-\pi^+\pi^-$	200	2.6
$B_{(s)} \to D_s\rho, D_s^*\pi$	3,300	3.4
total	8,800	–

Table 4.19: Hadronic signal yields in the full dataset.

decay sequence	S
$B_s \to D_s^- l^+ X$, $D_s^- \to \phi\pi^-$	29,600 ± 800
$B_s \to D_s^- l^+ X$, $D_s^- \to K^{*0}K^-$	22,000 ± 800
$B_s \to D_s^- l^+ X$, $D_s^- \to \pi^-\pi^+\pi^-$	9,900 ± 700
total	61,500 ± 1,300

Table 4.20: Semileptonic signal yields in the full dataset.

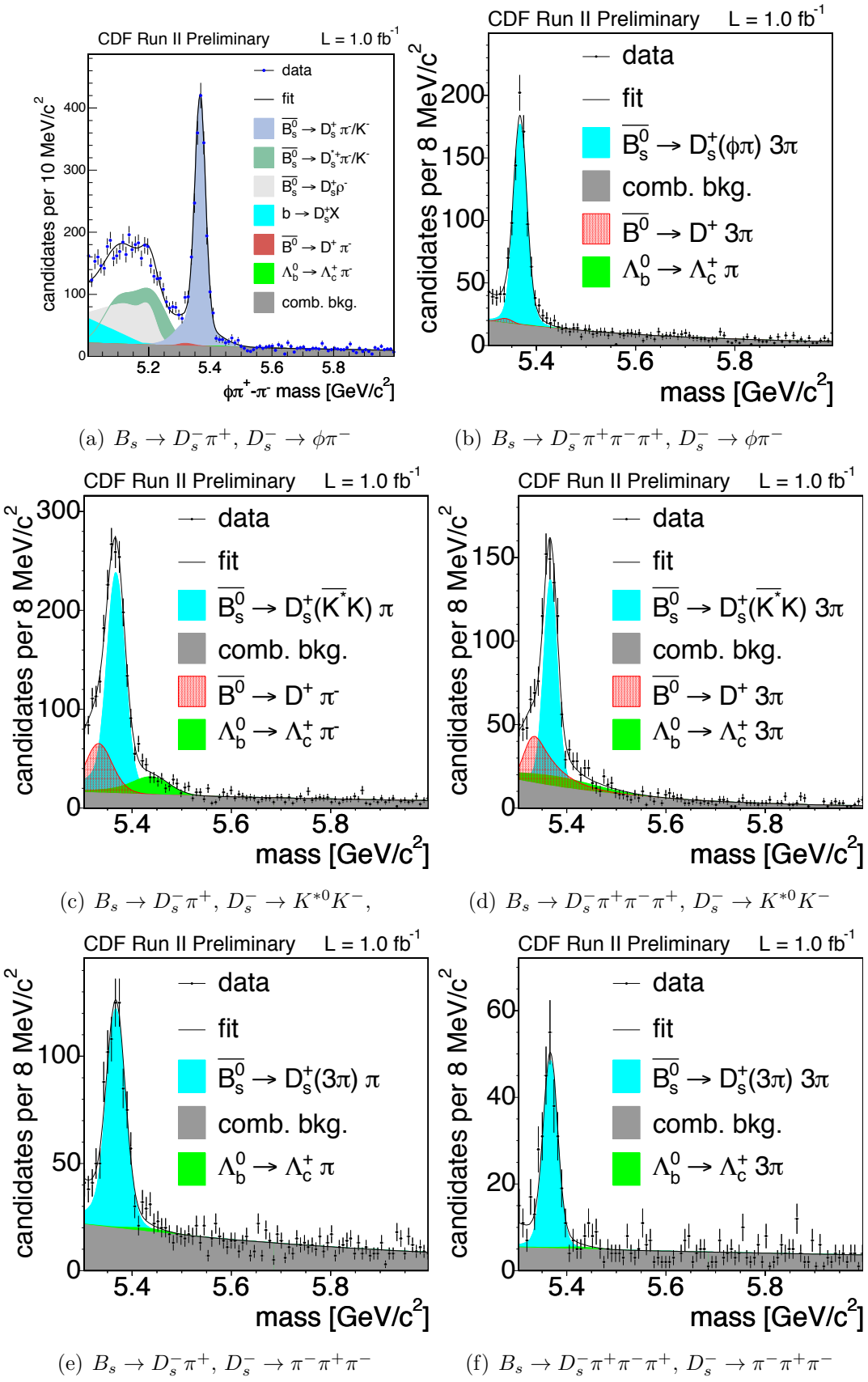

(a) $B_s \to D_s^- \pi^+$, $D_s^- \to \phi\pi^-$ (b) $B_s \to D_s^- \pi^+\pi^-\pi^+$, $D_s^- \to \phi\pi^-$

(c) $B_s \to D_s^- \pi^+$, $D_s^- \to K^{*0}K^-$, (d) $B_s \to D_s^- \pi^+\pi^-\pi^+$, $D_s^- \to K^{*0}K^-$

(e) $B_s \to D_s^- \pi^+$, $D_s^- \to \pi^-\pi^+\pi^-$ (f) $B_s \to D_s^- \pi^+\pi^-\pi^+$, $D_s^- \to \pi^-\pi^+\pi^-$

Figure 4.12: Mass distributions of the hadronic B_s modes in the full dataset.

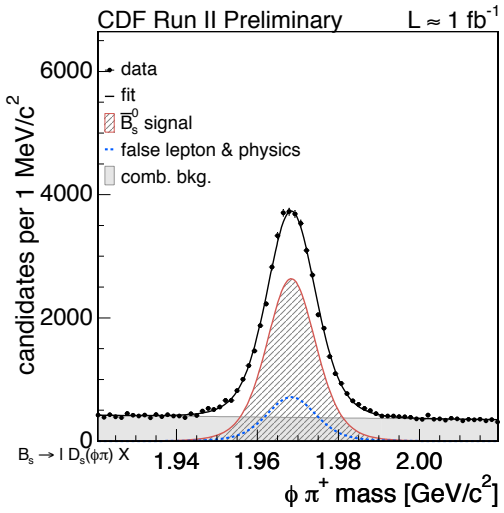

(a) $B_s \to D_s^- l^+ X$, $D_s^- \to \phi\pi^-$: $m(D_s)$

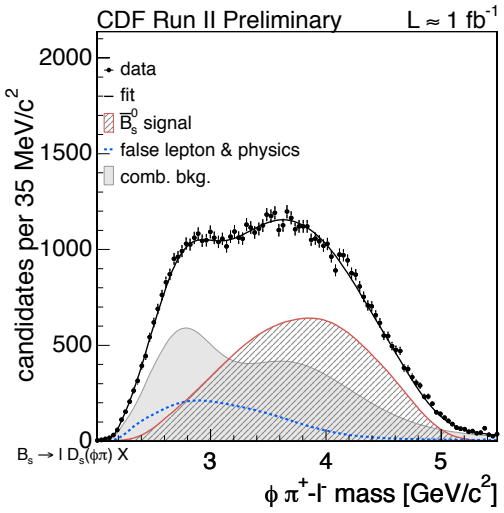

(b) $B_s \to D_s^- l^+ X$, $D_s^- \to \phi\pi^-$: $m(D_s l)$

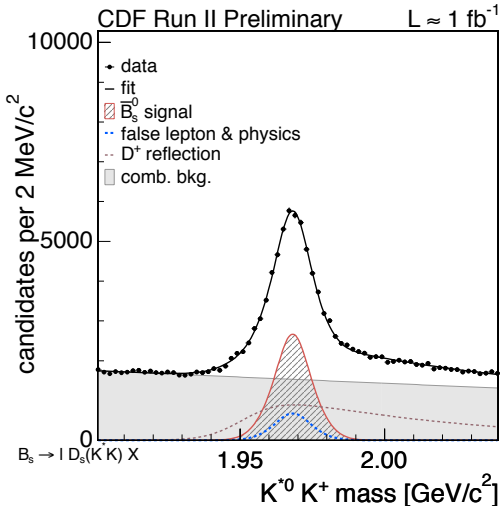

(c) $B_s \to D_s^- l^+ X$, $D_s^- \to K^{*0}K^-$: $m(D_s)$

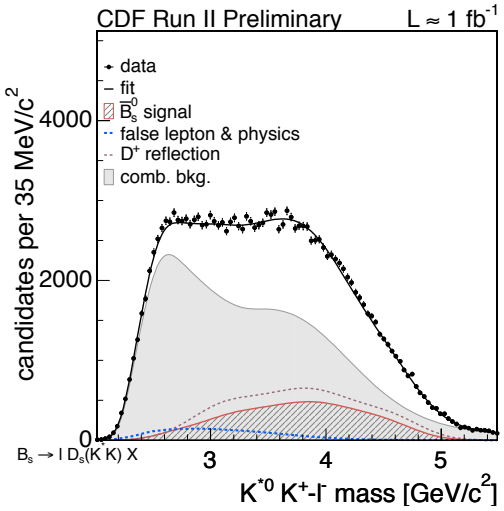

(d) $B_s \to D_s^- l^+ X$, $D_s^- \to K^{*0}K^-$: $m(D_s l)$

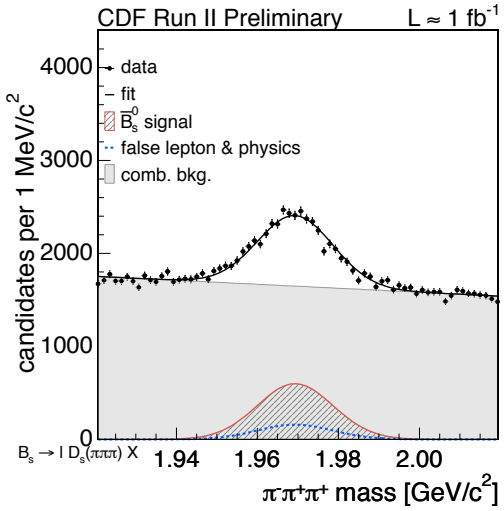

(e) $B_s \to D_s^- l^+ X$, $D_s^- \to \pi^-\pi^+\pi^-$: $m(D_s)$

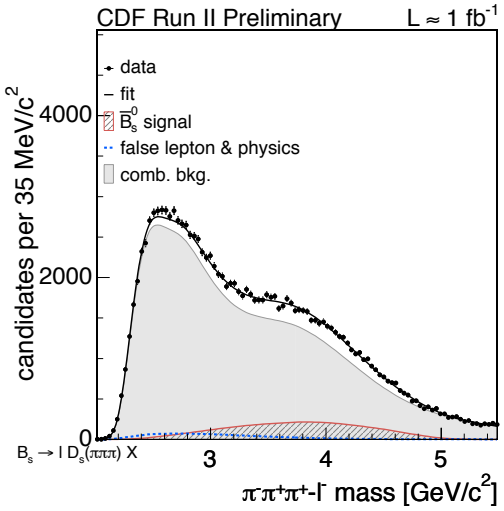

(f) $B_s \to D_s^- l^+ X$, $D_s^- \to \pi^-\pi^+\pi^-$: $m(D_s l)$

Figure 4.13: Mass distributions of the semileptonic B_s modes in the full dataset.

4.5 Monte Carlo samples

Samples of Monte Carlo simulated b-hadron decays are used at several stages along this dissertation. Their applications include the following: the estimation of the signal yields in the selection optimization procedure; the determination of data samples composition, as well as of characteristics of signal and physics type background components, such as mass and proper decay time distributions; reconstruction efficiencies, together with treatment of trigger, selection, and partial reconstruction effects on proper decay time distributions; testing of fitting framework.

A Monte Carlo sample is generated for each nominal B signal mode contributing to our data samples. Samples of additional b-hadron decays are also generated to estimate physics type backgrounds. These include exclusive samples where a single B meson decay chain is enforced, as well as inclusive samples where various B decays contributing to a common final state signature are included. As examples of the latter case we have: $B \to J/\psi X$ with $J/\psi \to \mu^+\mu^-$; $B \to \bar{D}^0 X$ with $\bar{D}^0 \to K^+\pi^-$; or $B^{+,0} \to D^- l\nu X$ with $D^- \to K^+\pi^-\pi^-$. In order to produce such generic inclusive samples in an efficient fashion only the desired decays are generated. This follows from the selection of the channels leading to a specified final state (such as the J/ψ or D meson modes mentioned) from a default global decay table, in which the relative branching ratios need to be re-evaluated [66].

Generation and decay of *b*-hadrons

For the generation and the fragmentation of b-quarks we employ the `Bgenerator` [67] Monte Carlo program. This is based on Next to Leading Order QCD calculations [68] and uses the Peterson fragmentation function [69]. The generation process involves a single b-quark, which then fragments to a b-hadron. No additional fragmentation products or proton remnants are present.

For simulating b-hadron decays we use the `EvtGen` [70] program, which has been extensively tuned by the experiments operating at the $\Upsilon(4S)$ resonance.

Realistic simulation

The detector response to the generated events is provided by the `Geant` [71] simulation framework, which models the detector geometry and the behavior of its active components at hit level. Time dependent detector inefficiencies, which arise for example from temporary disablement of subdetector components, are taken into account in the simulation, and the data taking period is simulated run-by-run with the event numbers per run calculated on the basis of the integrated luminosity of the run.

The data acquisition and trigger systems response is also simulated and the output of the simulation mimics the real raw data structure. Events are then passed through the production stage during which physics objects (*e.g.* tracks, leptons, jets, *etc*) are created. Finally, the simulated samples are stored in the form of `BStntuples` [55], and the analysis selection and reconstruction criteria are applied.

The agreement of relevant kinematic distributions obtained from the data and the simulated samples was validated. Where applicable, Monte Carlo reweighting was performed in order to account for run-by-run prescaling of the trigger paths.

4.6 Résumé

The selection and reconstruction criteria employed for collecting and forming the various data samples used in this dissertation have been presented.

The raw data selected by the online trigger system is sent for permanent storage, being then passed to the production stage where the most detailed calibrations and reconstruction algorithms are applied. Such datasets undergo further preparation, where the event tracks and vertices are refit and constructed under specific particle hypotheses. The collections of particle candidates – such as J/ψ, D, and B mesons – are pre-selected and stored in `BStntuples` which contain the candidates information. Optimized selection criteria requirements are then applied to form the final collection of B meson candidates. The relevant information, for the next stages of the analysis, pertaining to each individual B candidate is retrieved and appended to an `ascii` file; these selected data include mass, momentum, decay length, as well as flavor tagging information. For each decay sub-sample such a data file is constructed which contains the required input to be provided to the unbinned likelihood framework where the fits of the data are performed — which constitutes the subject of the following chapters. The sequence of data formats and steps may be summarily represented as

`Datasets` $\rightarrow$ `Pre-selection` $\rightarrow$ `BStntuple` $\rightarrow$ `Selection` $\rightarrow$ `Fit input file`.

The relative B meson signal yields for the various sample categories as extracted from the $355\,\mathrm{pb}^{-1}$ dataset are summarized as

	B^+	B^0	B_s
$J/\psi K$	5,000	1,800	–
$D\pi(\pi\pi)$	11,200	17,300	1,100
Dl	130,000	130,000	13,000

In the full 1 fb^{-1} dataset, the combined B_s signal yields for the (fully- and partially-reconstructed) hadronic modes is about 9,000 while about 62,000 semileptonic B_s signals are reconstructed.

The composition of the data samples has been studied, and the various signal and background components were assessed and characterized. This was achieved in part through the generation and use of Monte Carlo samples, which were described. These samples were used as well in the selection optimization procedure, and further provide necessary input to be employed in subsequent chapters.